

# Faculty of Physics and Astronomy

University of Heidelberg

Diploma thesis  
in Physics

submitted by  
**Aleksandra Adametz**  
born in Neustadt/Poland

January 2005



# **Preshower Measurement with the Cherenkov Detector of the *BABAR* Experiment**

*This diploma thesis has been carried out by Aleksandra Adametz at the  
Physical Institute  
under the supervision of  
Prof. Dr. Ulrich Uwer*

## Kurzfassung

In dieser Arbeit wird der Einfluss des Materials, das sich vor dem elektromagnetischen Kalorimeter befindet, auf die Energieauflösung von Photonen untersucht. 13% der Photonen wechselwirken vor allem mit dem Material des Tscherenkow-Detektors und bilden bereits vor dem Kalorimeter elektromagnetische Schauer. In dieser Arbeit wird der Tscherenkow-Detektor zur Identifizierung dieser „Prä-Schauer“ verwendet. Die im „Prä-Schauer“ gebildeten Elektron- und Positronpaare emittieren im Material des Tscherenkow-Detektors Tscherenkow-Licht. Die nachgewiesenen Tscherenkow-Photonen werden den im Kalorimeter gemessenen Photonen zugeordnet. Die Anzahl der assoziierten Tscherenkow-Photonen wird verwendet, um „Prä-Schauer“ zu identifizieren.

Effizienz und Untergrund der Methode werden auf simulierten Daten bestimmt. „Prä-Schauer“ können mit einer Effizienz von 50% detektiert werden. Photonen ohne „Prä-Schauer“ werden bei einem Untergrund von 7% selektiert. Die Ergebnisse aus der Simulationsstudie können auf Strahl-daten bestätigt werden. Wenn nur Photonen ohne „Prä-Schauer“ benutzt werden, ergibt sich eine relative Verbesserung der Massenauflösung von 5%. In einem weiteren Schritt wird der Energieverlust über die Zahl der detektierten Tscherenkow-Photonen gemessen und die vom Kalorimeter gemessene Energie korrigiert.

## Abstract

This thesis studies the impact of the material in front of the electromagnetic calorimeter on the photon energy resolution. 13% of the photons interact mainly with the material of the Cherenkov detector and start electromagnetic showers already in front of the calorimeter. In this thesis the Cherenkov detector is used to identify these “preshowers.” The electrons and positrons of the “preshower” emit Cherenkov light in the material of the Cherenkov detector. The detected Cherenkov photons are associated to photons measured in the calorimeter. The number of associated Cherenkov photons is used to identify “preshowers”.

Efficiency and background of the method are determined on simulated data. “Preshowers” can be detected with an efficiency of 50%. Photons without “preshowers” are selected with a “preshower” background of 7%. The results from the simulation studies can be confirmed on beam-data. If only photons without “preshowers” are used, a relative improvement of 5% can be obtained for  $\pi^0 \rightarrow \gamma\gamma$  decays. In a further step, the energy loss is measured with the number of detected Cherenkov photons and the energy measured in the calorimeter is corrected.

# Contents

<b>1</b>	<b>Chapter 1</b>	<b>7</b>
1.1	Introduction . . . . .	7
<b>2</b>	<b>Theoretical background</b>	<b>9</b>
2.1	The Standard Model of Particle Physics . . . . .	9
2.2	Quark mixing matrix . . . . .	10
2.3	B-meson system . . . . .	10
2.4	$\pi^0$ -mesons . . . . .	12
2.5	Interactions of particles with matter . . . . .	12
2.5.1	Charged particles . . . . .	12
2.5.2	Photons . . . . .	14
2.5.3	Electromagnetic showers . . . . .	14
<b>3</b>	<b>The BaBar experiment</b>	<b>17</b>
3.1	The PEP-II collider . . . . .	17
3.2	Components of the BaBar Detector . . . . .	18
3.2.1	SVT . . . . .	18
3.2.2	DCH . . . . .	20
3.2.3	Magnet Coil and IFR . . . . .	20
3.3	DIRC . . . . .	22
3.3.1	Purpose and layout . . . . .	22
3.4	Electromagnetic calorimeter . . . . .	25
3.4.1	Purpose and layout . . . . .	25
3.4.2	Clusters and bumps . . . . .	25
3.4.3	Calibration . . . . .	26
3.4.4	Material in front of the EMC . . . . .	28
3.5	Simulation and data sample . . . . .	28
<b>4</b>	<b>Preshower detection with the DIRC</b>	<b>31</b>
4.1	Photon showers . . . . .	31
4.2	Cherenkov photons and calorimeter clusters . . . . .	35
4.3	Selection of clusters . . . . .	42
4.4	Selection of detected Cherenkov photons . . . . .	43

4.5	Identification of preshowers . . . . .	47
4.5.1	Definition of detected preshowers . . . . .	47
4.5.2	Definition of efficiency and pollution . . . . .	47
4.5.3	Optimization of the preshower detection . . . . .	48
4.6	Summary . . . . .	54
<b>5</b>	<b>Preshower corrections</b>	<b>55</b>
5.1	Impact of preshowers on the photon energy resolution . . . . .	55
5.1.1	Fitting procedure . . . . .	55
5.1.2	Photon energy resolution . . . . .	57
5.2	Energy correction . . . . .	61
5.2.1	Binning . . . . .	61
5.2.2	Determination of correction coefficients . . . . .	63
5.2.3	Verification . . . . .	68
5.2.4	Impact on the photon energy resolution . . . . .	68
5.3	Comparison of data with simulation . . . . .	72
5.3.1	$\pi^0$ mass distribution . . . . .	72
5.3.2	$\pi^0$ -mesons with preshowers . . . . .	73
5.3.3	Preshower identification in data and simulation . . . . .	74
5.3.4	Energy correction in data and simulation . . . . .	79
5.4	Summary . . . . .	82
<b>6</b>	<b>Conclusion and outlook</b>	<b>83</b>
6.1	Conclusion . . . . .	83
6.2	Outlook . . . . .	83

# Chapter 1

# Chapter 1

## 1.1 Introduction

The Standard Model of Particle Physics provides an excellent description of the present knowledge of the fundamental particles and their interactions. The predictions deduced from the model are confirmed by many experiments. However, there are still some open questions. One example is the violation of the CP symmetry which is known since 1964. J.W. Cronin and Val Fitch found in the neutral kaon system that the CP symmetry is violated [1]. The CP violation predicted from the Standard Model is not large enough to explain the asymmetry of matter and antimatter in universe. Thus, the precise measurement of CP violating systems is very important to test the validity of the Standard Model. The main physics goal of the *BABAR* experiment is to study CP violation in B-meson systems. A precise and efficient measurement of B-mesons and their decay products is necessary to achieve the physics goals. Since neutral pions are abundant in B-meson decays, the detection of  $\pi^0$ -mesons is very important. Neutral pions decay into two photons (branching fraction:  $(98.798 \pm 0.032)\%$  [2]) which need to be detected with high efficiency and energy resolution in the electromagnetic calorimeter (EMC) of the *BABAR* detector.

The energy resolution of the EMC is degraded by energy losses in front of the EMC. These energy losses are due to the interaction of photons with the material of inner detector sub-systems. Electromagnetic showers may start before the photon reaches the EMC, these showers are called preshowers. In Chapter 4 it will be shown that preshowers are mainly starting in the Cherenkov device (DIRC) which is located directly in front of the calorimeter. This diploma thesis aims to identify photon showers with a preshower fraction in front of the calorimeter. For the identification the Cherenkov detector of *BABAR* is used. The  $e^+e^-$ -pairs in the shower emit Cherenkov light which is detected by the DIRC. In this thesis, these Cherenkov photons will be associated to clusters measured in the calorimeter to identify preshowers. The number of detected Cherenkov photons assigned to a cluster will be used to decide whether a photon started to shower in front of the

EMC or not. The identification algorithm will be optimized to achieve a high efficiency and low misidentification.

In Chapter 5 the impact of preshowers on the photon energy resolution will be studied by measuring and comparing the energy resolution of clusters with and without preshowers. Furthermore, a method to correct the energy loss in preshowers is developed. The number of associated Cherenkov photons is correlated to the energy loss in the preshower. Possible improvements on the photon energy resolution will be discussed. Finally, both approaches, rejection of clusters with preshowers and energy correction, are verified to yield consistent results of clusters on Monte Carlo simulations and real data by measuring the width of the  $\pi^0$  mass distribution.

# Chapter 2

## Theoretical background

### 2.1 The Standard Model of Particle Physics

The Standard Model of Particle Physics describes the fundamental particles and three of the four known interactions, the electromagnetic, the weak and the strong force. The fourth interaction, gravity, is not included in the Standard Model. The electromagnetic and the weak force are unified to the electro-weak interaction. All fundamental particles are divided into two groups, the fermions as the building blocks of matter and the bosons as the force carriers. They are summarized in Table 2.1 and Table 2.2. Whereas all particles are subject to the weak interaction, only charged particles feel the electromagnetic force and only colored particles, that means quarks are affected by the strong interaction.

	$Q/e$	$I$	$I_3$	$Y$	$C$	
<b>Quarks</b>						
$\begin{pmatrix} u \\ d' \end{pmatrix}_L$	$\begin{pmatrix} c \\ s' \end{pmatrix}_L$	$\begin{pmatrix} t \\ b' \end{pmatrix}_L$	$\frac{2}{3}$ $-\frac{1}{3}$	$\frac{1}{2}$ $-\frac{1}{2}$	$+\frac{1}{6}$ $+\frac{1}{6}$	r,g,b
$u_R$	$c_R$	$t_R$	$\frac{2}{3}$	0	$\frac{2}{3}$	r,g,b
$d_R$	$s_R$	$b_R$	$-\frac{1}{3}$	0	$-\frac{1}{3}$	r,g,b
<b>Leptons</b>						
$\begin{pmatrix} e \\ \nu_e \end{pmatrix}_L$	$\begin{pmatrix} \mu \\ \nu_\mu \end{pmatrix}_L$	$\begin{pmatrix} \tau \\ \nu_\tau \end{pmatrix}_L$	-1 0	$\frac{1}{2}$ $+\frac{1}{2}$	$-\frac{1}{2}$ $-\frac{1}{2}$	w
$e_R$	$\mu_R$	$\tau_R$	-1	0	-1	w

**Table 2.1:** *Fundamental particles of the Standard Model: The fermions are characterized by the charge  $Q$ , the weak isospin  $I$  (its third component  $I_3$ ), the hyper charge  $Y$  and the color charge  $C$  which has three possible values called red ( $r$ ), green ( $g$ ) and ( $b$ ). Color neutral particles are denoted with a “w”.*

Interaction	Mediating Boson
electro-magnetic	photon ( $\gamma$ )
weak	$W^+$ , $W^-$ , $Z^0$
strong	gluon ( $g_{1\dots 8}$ )

**Table 2.2:** *Fundamental Particles of the Standard Model: The vector bosons are the mediators of the interactions.*

## 2.2 Quark mixing matrix

In the Standard Model, the quark mass eigenstates  $q$  are not the same as the weak eigenstates  $q'$ . They are related by the *Cabibbo-Kobayashi-Maskawa Matrix* ( $V_{i,j}$ ) [3] :

$$\begin{pmatrix} d' \\ s' \\ b' \end{pmatrix} = \begin{pmatrix} V_{ud} & V_{us} & V_{ub} \\ V_{cd} & V_{cs} & V_{cb} \\ V_{td} & V_{ts} & V_{tb} \end{pmatrix} \cdot \begin{pmatrix} d \\ s \\ b \end{pmatrix}. \quad (2.1)$$

The elements  $V_{ij}$  of the mixing matrix describe the probability for a transition of a quark  $q_i$  into a quark  $q_j$ . Measurements of the matrix elements show that the diagonal elements are close to one, that means transitions within a generation are preferred. Due to probability conservation the CKM-matrix is unitary:

$$VV^\dagger = V^\dagger V = 1 \quad (2.2)$$

Using the unitarity relation and an appropriate choice of the absolute quark phases, the 18 parameters of the complete matrix can be reduced to 4 real parameters, three angles and one phase. The finite phase is the source of the violation of the CP symmetry in the Standard Model. Equation 2.2 provides relations between the matrix elements  $V_{i,j}$ . The most important one is:

$$V_{ud}V_{ub}^* + V_{cd}V_{cb}^* + V_{td}V_{tb}^* = 0 \quad (2.3)$$

It can be represented by a triangle in the complex plane with the following angles.

$$\begin{aligned} \alpha &= \arg\left(-\frac{V_{td}V_{tb}^*}{V_{ud}V_{ub}^*}\right), \quad \beta = \arg\left(-\frac{V_{cd}V_{cb}^*}{V_{td}V_{tb}^*}\right), \\ \gamma &= \arg\left(-\frac{V_{ud}V_{ub}^*}{V_{cd}V_{cb}^*}\right) = \pi - \alpha - \beta \end{aligned} \quad (2.4)$$

This so called unitarity triangle is shown in Fig 2.1. The triangle area provides a measure of the CP violation.

## 2.3 B-meson system

The main goal of the *BABAR* experiment is the measurement of CP violation in the B-meson system. The mesons  $B^0 = |d\bar{b}\rangle$  and  $\bar{B}^0 = |\bar{d}b\rangle$  are eigenstates

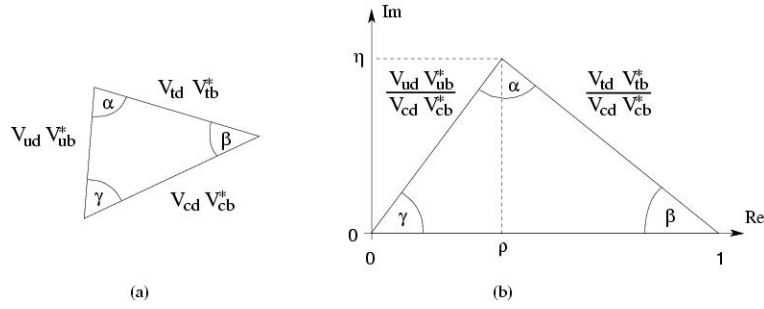


**Figure 2.1:** *The unitarity triangle. (a) shows the orthogonality condition between the first and third column of the Cabbibo-Kobayashi-Maskawa Matrix. (b) The triangle has been rescaled. The base has unit length.*

of the strong interaction (*flavor* eigenstates). However, in weak interactions, transitions between  $B^0$  and  $\bar{B}^0$  are possible. The mass eigenstates  $B_L^0$  and  $B_H^0$  with the masses  $m_L$ ,  $m_H$  and the decay widths  $\Gamma_L$ ,  $\Gamma_H$ , are a mixture of the above flavor eigenstates. The subscripts  $L$  and  $H$  stand for *light* and *heavy*.

$$\begin{aligned} |B_L\rangle &= p|B^0\rangle + q|\bar{B}^0\rangle & \text{and} \\ |B_H\rangle &= p|B^0\rangle - q|\bar{B}^0\rangle \end{aligned} \quad (2.5)$$

with

$$|p|^2 + |q|^2 = 1. \quad (2.6)$$

Standard Model calculations relate the parameters  $p$  and  $q$  to two elements of the CKM-matrix:

$$\frac{q}{p} = \frac{V_{td}V_{tb}^*}{V_{td}^*V_{tb}} \quad (2.7)$$

The time development of the *flavor* eigenstates is given by:

$$\begin{aligned} |B^0, t\rangle &= f_+(t)|B^0\rangle + \frac{q}{p}f_-(t)|\bar{B}^0\rangle \\ |\bar{B}^0, t\rangle &= f_+(t)|\bar{B}^0\rangle + \frac{p}{q}f_-(t)|B^0\rangle \end{aligned} \quad (2.8)$$

with

$$\begin{aligned} f_+(t) &= \exp(-\Gamma \frac{t}{2}) \exp(-imt) \cos(\Delta m \frac{t}{2}) \\ f_-(t) &= \exp(-\Gamma \frac{t}{2}) \exp(-imt) i \sin(\Delta m \frac{t}{2}) \end{aligned} \quad (2.9)$$

where the definitions  $m = (m_H + m_L)/2$  and  $\Delta m = m_H - m_L$  are used. Since the lifetimes of the two mass eigenstates are very similar, the difference between

$\Gamma_L$  and  $\Gamma_H$  is negligible:  $\Gamma = \Gamma_L \approx \Gamma_H$ . The CP asymmetry  $a_{CP}(t)$  is defined as follows.

$$a_{CP}(t) = \frac{\Gamma(B^0(t) \rightarrow f_{CP}) - \Gamma(\bar{B}^0(t) \rightarrow f_{CP})}{\Gamma(B^0(t) \rightarrow f_{CP}) + \Gamma(\bar{B}^0(t) \rightarrow f_{CP})}$$

where  $f_{CP}$  are CP eigenstates. An example of a B-meson decay channel which is well suited to measure CP violation is the so called *golden decay*:

$$\begin{aligned} B^0 &\rightarrow J/\psi K_S^0 \\ \bar{B}^0 &\rightarrow J/\psi K_S^0 \end{aligned}$$

In this case the measurement of the CP asymmetry allows the determination of  $\sin(2\beta)$

$$a_{CP}(t) = -\sin(2\beta) \sin(\Delta mt) . \quad (2.10)$$

Since a large fraction of B-mesons decays via fully hadronic or semileptonic modes,  $\pi^0$ -mesons are abundant in B-decays and thus at the *BABAR* experiment. The precise measurement of  $\pi^0$ -mesons is hence crucial to the analysis of the B-meson system.

## 2.4 $\pi^0$ -mesons

$\pi^0$ -mesons decay via the electromagnetic interaction. The dominant decay channel is  $\pi^0 \rightarrow \gamma\gamma$  with a branching ratio of  $(98.798 \pm 0.032)\%$ . Due to its short lifetime  $\tau = (8.4 \pm 0.6) \cdot 10^{-17}$  s, its free path length is of the order of a few nm. It can, thus, only be detected by the measurement of its decay products. The measurement of the photon energy  $E_\gamma$  and of the angle  $\alpha$  between the photon propagation directions allows to reconstruct the  $\pi^0$  mass  $m_{\pi^0}$ :

$$m_{\pi^0}^2 = 2E_{\gamma,1}E_{\gamma,2}(1 - \cos \alpha) . \quad (2.11)$$

Within the *BABAR* experiment, photons are detected via electromagnetic showers measured with the calorimeter described in Section 3.4.

## 2.5 Interactions of particles with matter

The aim of this thesis is to study the impact of material in front of the electromagnetic calorimeter on the photon energy resolution. Hence, particle interactions with matter are essential for this study.

### 2.5.1 Charged particles

#### Ionization

When passing through a medium, charged particles lose energy by transferring momentum to an atomic electron [4]. The Bethe-Bloch formula gives the average

energy loss for ionization and excitation:

$$-\frac{dE}{dx} = 4\pi \frac{z^2 \alpha^2}{\beta^2} \frac{Z\rho}{Am_N m_e} \left( \frac{1}{2} \ln \frac{2m_e \beta^2 \gamma^2 T_{max}}{I^2} - \beta^2 - \frac{\delta}{2} \right) \quad (2.12)$$

where  $m_e$ ,  $m_N$ ,  $\alpha$  are the electron and nucleon masses and the fine structure constant. The incoming particle properties are the charge  $z$ , the velocity  $\beta$  and the gamma factor  $\gamma$ .  $Z$ ,  $A$ ,  $\rho$  and  $I$  are the charge and atomic number of the atoms of the medium, the density and average ionization potential for the medium.  $\delta$  is a small correction due to medium polarization. The typical value of minimal energy losses at  $\beta\gamma = 2$  is about 2 MeV/(g/cm<sup>2</sup>).

### Scintillation

A charged particle traversing matter leaves excited molecules behind it. Certain types of molecules, release a small fraction of this energy in the form of photons. The amount of energy carried away by scintillation light is typically 1% or less of  $dE/dx$ . This light is used to measure electromagnetic showers in the calorimeter of the *BABAR* detector.

### Bremsstrahlung

Relativistic charged particles experience accelerations when propagating through matter. These accelerations are due to multiple scattering on nuclei. The energy loss is proportional to the energy of the incoming particle.

$$-\frac{dE}{dx} = \frac{E}{X_0} \quad (2.13)$$

The proportionality coefficient  $X_0$  is called the radiation length. It depends on the material properties and the mass and charge of the incoming particle.

### Cherenkov radiation

A charged particle which traverses a dielectric medium emits Cherenkov light if its velocity is larger than the speed of light in the considered material. The atoms in the medium are temporarily polarized by the dipole field along the particle trajectory axis. This causes the atoms to radiate short electromagnetic pulses. The emitted light forms a coherent wavefront. This radiation is only observed at a particular ‘‘Cherenkov’’ angle  $\Theta_C$ , with respect to the track of the particle:

$$\cos \Theta_C = \frac{1}{n(\lambda)\beta} \quad (2.14)$$

where  $\lambda$  is the wave length of the emitted radiation and  $n$  is the refractive index of the medium. The number of photons emitted by a particle of charge  $Q = ze$

per unit path length and per unit wave length is equal to:

$$\frac{dN^2}{dx d\lambda} = \frac{2\pi\alpha z^2}{\lambda^2} \cdot \left(1 - \frac{1}{\beta^2 \cdot n^2(\lambda)}\right) \quad (2.15)$$

where  $\alpha = \frac{e^2}{\hbar c} = \frac{1}{137}$  is the fine structure constant.

## 2.5.2 Photons

### Photoelectric process

This is the process of photo absorption leading to ionization of an atom. If the photon energy is sufficiently large an electron from the inner atomic shells is emitted. In this case an electron from an outer shell can fall into the free place and emit light with a characteristic frequency. This effect dominates at low photon energies.

### Compton effect

In this process, photons scatter on free electrons. Since the binding energy of atomic electrons is low compared to the energy of passing relativistic particles, this process is also relevant for particles traversing through matter.

### Pair production

Photons produce  $e^+e^-$ -pairs in nuclear fields. The photon energy needs to be larger than twice the mass of an electron:  $E_\gamma \geq 2m_e \approx 1\text{MeV}$ . In the high-energy limit, the cross section for the pair-production is given by:

$$\sigma = \frac{7}{9}(A/X_0 N_A) \quad (2.16)$$

where  $A$  is the atomic number and  $N_A$  Avogadro's Number. This equation is applicable down to energies as low as 1 GeV.

## 2.5.3 Electromagnetic showers

The principle of an electromagnetic calorimeter is based on the measurement of electromagnetic showers which are induced by photons due to the interaction with the calorimeter material. A high-energy photon traversing matter converts into an electron-positron pair which then emits photons via bremsstrahlung. These secondary photons convert into further  $e^+e^-$ -pairs. Thus, the number of shower particles increases exponentially. This process continues until the energy of the electrons falls below the critical energy  $E_c$ . Then other processes than bremsstrahlung start to dominate: The  $e^+e^-$  pairs lose their energy via ionization and excitation.

The shower maximum  $t_{max}$  of the longitudinal profile of the energy deposition is given by Equation 2.17. It is measured in units of radiation length  $X_0$ .

$$t_{max} = \ln\left(\frac{E}{E_c}\right) + C_i \quad i = e, \gamma \quad (2.17)$$

where  $E$  is the energy of the incident particle,  $C_e = -0.5$  for electron-induced showers and  $C_\gamma = +0.5$  for photon-induced electromagnetic showers.

The transverse spread of a shower is mainly caused by multiple scattering. It is described by the Molière radius  $R_m$ .

$$R_m = \frac{E_S}{E_c} X_0 \quad (2.18)$$

where  $E_S \approx 21 \text{ MeV}$ . On the average, 99% of the energy are contained inside a cone with a radius of  $3.5R_m$  around the direction of the incident particle. The transverse dimensions of the crystals in the *BABAR* calorimeter are equal to the Molière radius  $R_m=3.8 \text{ cm}$  of the calorimeter material. The crystal size is adequate to measure fully contained showers (see Section 3.4).



# Chapter 3

## The BaBar experiment

The *BaBar* experiment is located at the PEP-II  $e^+e^-$  collider of the Stanford Linear Accelerator Center (SLAC) in Palo Alto near San Francisco (CA, USA). Its detector [5] is designed to provide optimal conditions to study the CP-violation in B-mesons systems [6]. Beyond this primary goal a large number of other related topics can be investigated.

### 3.1 The PEP-II collider

The PEP-II  $e^+e^-$ -collider (Figure 3.1) consists of two individual storage rings with a circumference of 2.2 km each. Positrons and electrons are accelerated with the linear accelerator (LINAC) to a nominal energy of 3.1 GeV and 9.0 GeV, respectively. They are injected into the *Low Energy Ring* (LER) and the *High Energy Ring* (HER). The interaction region is surrounded by the *BaBar* detector. Since the positron and electron energies are not equal, the center-of-mass system

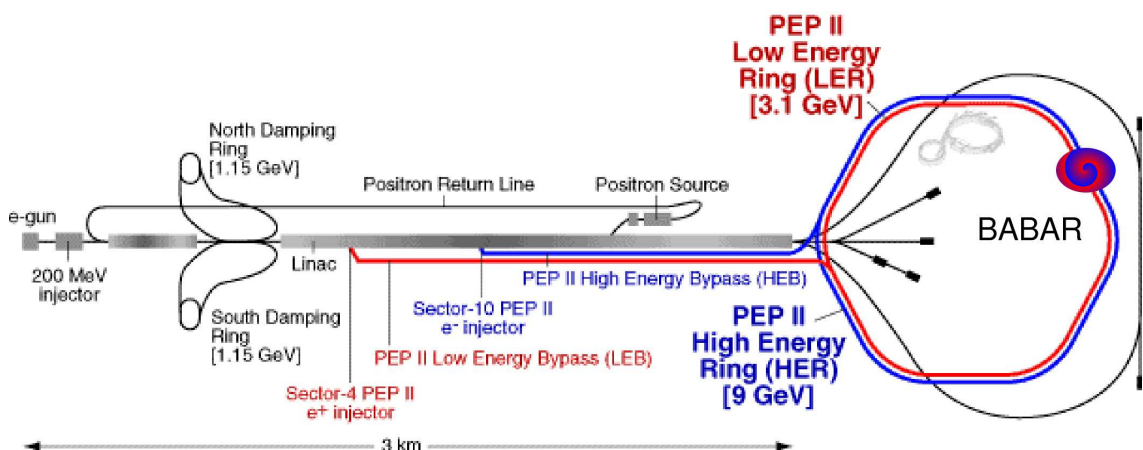


Figure 3.1: PEP-II: electron positron collider situated at SLAC.

is boosted with a boost factor  $\beta\gamma = 0.56$ . The center-of-mass energy of 10.58 GeV corresponds to the mass of the  $\Upsilon(4S)$  resonance. The  $\Upsilon(4S)$  resonance decays mainly in  $B\bar{B}$ -pairs with a branching fraction of more than 96 %. Because of the small branching ratios of B-mesons to the interesting CP eigenstates which are of the order of  $10^{-4}$  a high luminosity is required. The design goal of PEP-II was a luminosity of  $3 \cdot 10^{33} \text{cm}^{-2}\text{s}^{-1}$ . The achieved luminosity is more than a factor three higher.

## 3.2 Components of the BaBar Detector

The *BABAR* detector is located at the crossing point of the two PEP-II storage rings. Because of the boosted center-of-mass system, the detector is asymmetric. The interaction point is not in the geometrical center of the detector. It is shifted towards the backward direction which is defined by the outgoing high-energy electron beam. Figure 3.2 shows an overview of the *BABAR* detector. The components of the *BABAR* detector are radially arranged. The Silicon Vertex Tracker (SVT) is located close to the beam pipe. The second tracking device is the Drift Chamber (DCH). The next component is the Detector of Internally Reflected Cherenkov Light (DIRC) which is mainly used to identify  $\pi$ -mesons and kaons. Its photon detection system is located at the backward end of the BaBar detector. The Electromagnetic Calorimeter (EMC) is the last sub-detector within the super-conducting magnet coil. The Instrumented Flux Return (IFR) is the outermost component.

### 3.2.1 SVT

The Silicon Vertex Tracker (Figure 3.3) is one of the two tracking devices of the *BABAR* detector. In order to measure the time-dependent CP asymmetry it is necessary to reconstruct precisely the tracks and decay vertices of charged particles. Many products of B-meson decays have a low transverse momentum  $p_t$ . The SVT is designed to measure  $p_t$  down to 50 MeV. It is located within the 4.5 m long support tube close to the beam pipe and consists of five layers of double-sided silicon strip detectors. The innermost layer has a radius of 32 mm. The radius of the fifth layer is 144 mm. The SVT covers the polar angle region from  $20^\circ$  to  $150^\circ$ . The three inner layers are critical for the measurement of the secondary vertices for the B-meson decays. The two outer layers are important for the pattern recognition and the low  $p_t$  tracking. The arrangement of the strip sensors along the beam direction as well as perpendicular to it allows the spatial measurement of the track directions and angles with a high resolution.

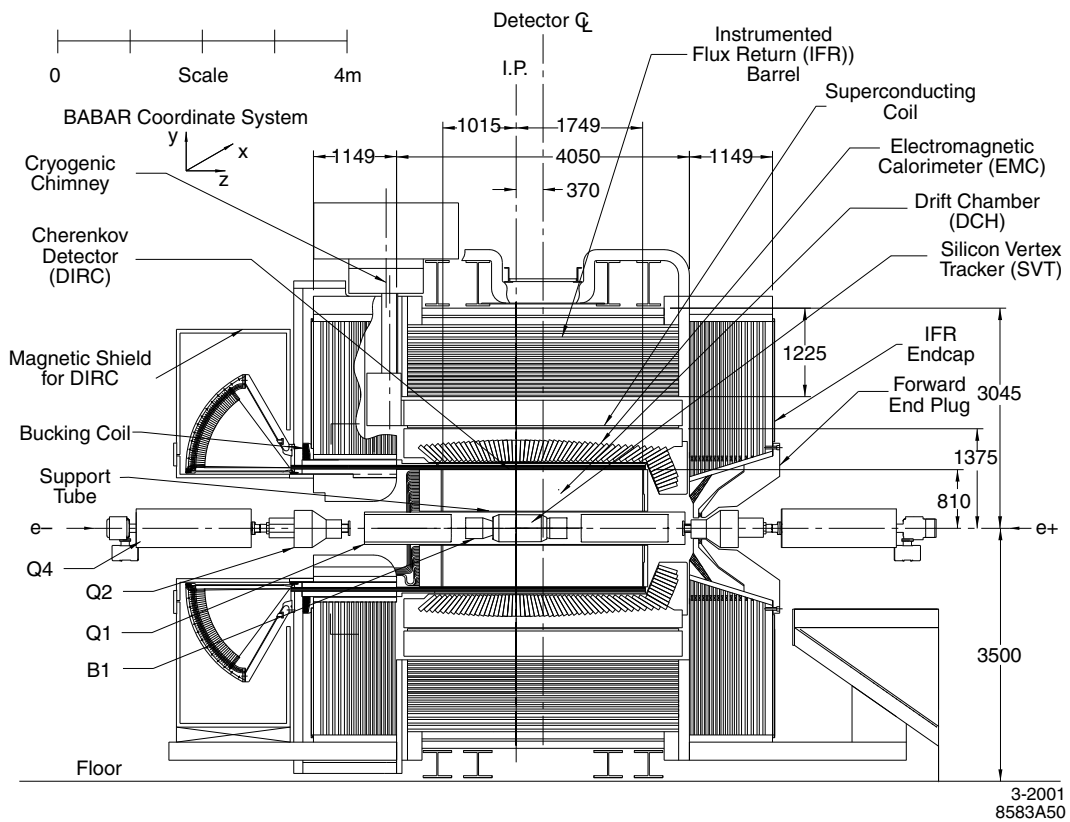


Figure 3.2: Longitudinal view of the BABAR detector.

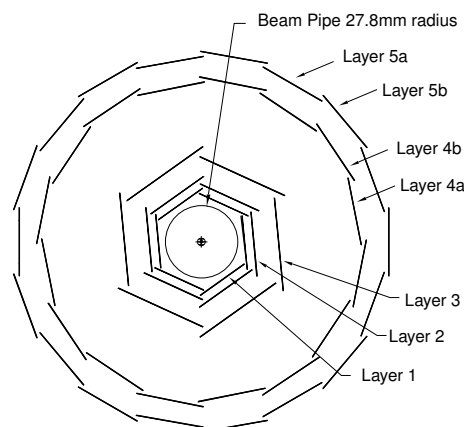


Figure 3.3: Transverse section of the SVT. The five layers of double-sided silicon strip detectors are shown schematically.

### 3.2.2 DCH

The Drift Chamber (Figure 3.4) allows the reconstruction of tracks with a transverse momentum above 100 MeV. Particle identification information can be obtained from the measurement of  $dE/dx$ . The discrimination of particles with different masses is complementary to that of the DIRC in the barrel region. The DCH is a multi-wire chamber with an inner radius of 26.6 cm and an outer radius of 80.9 cm. Its length is 280 cm. The DCH is composed of 40 layers with small hexagonal cells. In 24 of the layers, the wires are placed at small angles with respect to the  $z$ -axis. This provides additional longitudinal position information. The 20  $\mu\text{m}$ -thick sense wires consist of tungsten-rhenium. The aluminium field wires have a diameter of 80  $\mu\text{m}$  and 120  $\mu\text{m}$ , respectively. All wire are gold plated. The drift gas is a mixture of helium and isobutane in a ratio of 80 : 20.

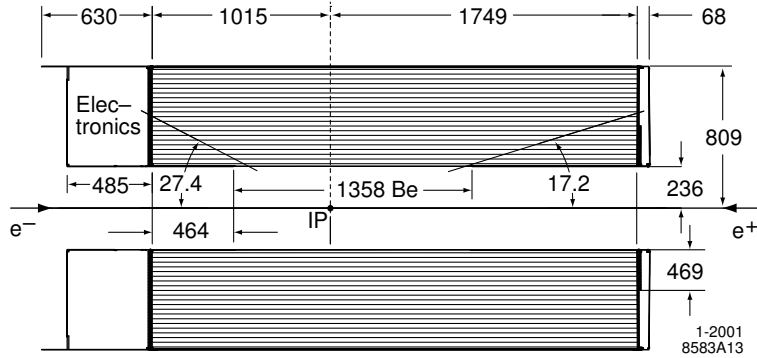
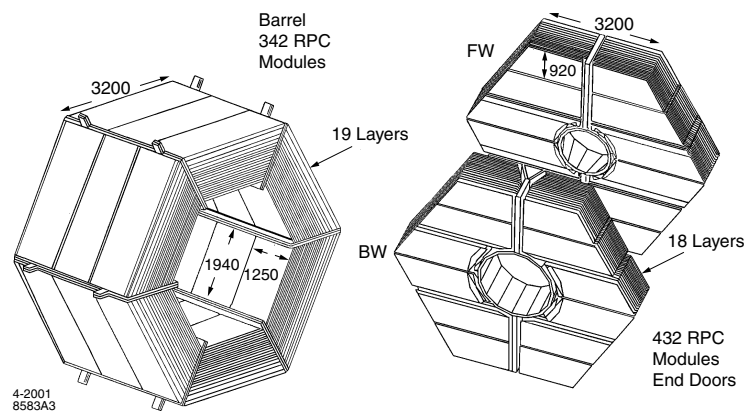


Figure 3.4: Longitudinal view of the Drift Chamber.

### 3.2.3 Magnet Coil and IFR

All inner detector components are surrounded by a super-conducting magnet coil. The coil has a weight of 6.5 t, an inner radius of 1.40 m and an outer radius of 1.73 m. It creates a 1.5 T magnetic field in parallel to the beam axis which allows the measurement of momenta from the track curvature.

The instrumented flux return (IFR) (Figure 3.5), the outermost detector component, consists of three major parts, the barrel sector and the forward and backward enddoors. It is built out of 18 steel plates which are instrumented with resistive plate chambers (RPC). The RPC layers which are located in gaps between the steel plates are filled with a gas mixture of argon, freon and a small fraction of isobutane. The IFR is designed to identify muons and neutral hadrons with a long decay time like  $K_L^0$  and neutrons.



**Figure 3.5:** Barrel sectors and forward and backward end doors of the IFR.

### 3.3 The Detector of Internally Reflected Cherenkov Light

#### 3.3.1 Purpose and layout

The Detector of Internally Reflected Cherenkov Light (DIRC) (Figure 3.6) is the most important particle identification device of the *BABAR* detector. It is used to separate  $\pi^0$ -mesons and kaons from B-meson decays. The discrimination of the particles is possible up to momenta of 4 GeV. The DIRC is a ring imaging Cherenkov detector with a new geometrical design concept.

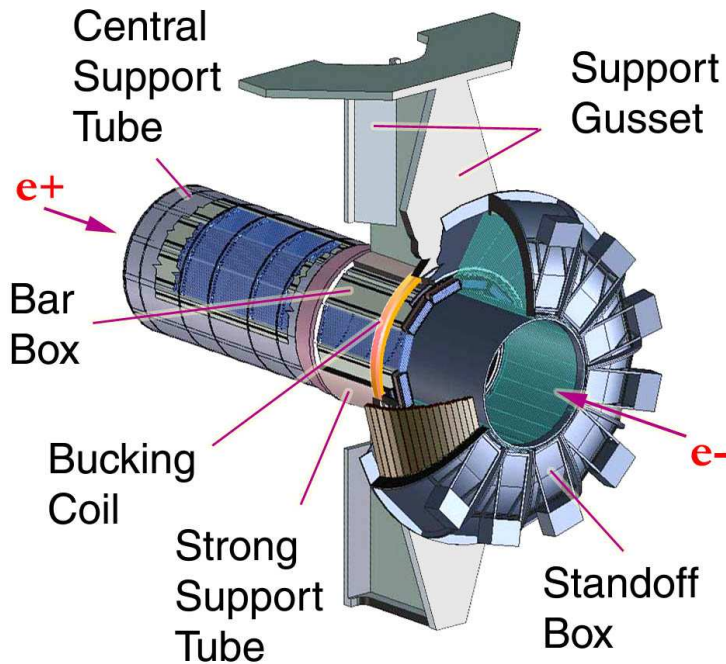


**Figure 3.6:** A schematic overview of the DIRC

The DIRC consists of 144 bars made of synthetic, fused silica with a mean refractive index  $n = 1.473$ . The bars have a rectangular cross-section and are 17 mm thick, 35 mm wide and 4.9 m long. Each bar is optically isolated from the neighboring bar by a  $150 \mu\text{m}$  air gap. The bars are contained in twelve *bar boxes* which are arranged in a polygonal barrel. The DIRC bars are used both as radiators and light pipes (Figure 3.7). Charged particles which traverse the DIRC-bars emit Cherenkov light in the angle  $\Theta_C$  with respect to the direction of the particle track which is reconstructed in the tracking sub-systems. The relation between the Cherenkov angle  $\Theta_C$  and the mass  $m$  and momentum  $p$  of

the particle is described by

$$\cos \Theta_C = \frac{1}{n} \sqrt{1 + \left(\frac{m}{p}\right)^2} = \frac{1}{n\beta} . \quad (3.1)$$

Many of the emitted Cherenkov photons are trapped by internal reflection and transported to the rear or forward end of the bar. The forward ends of the

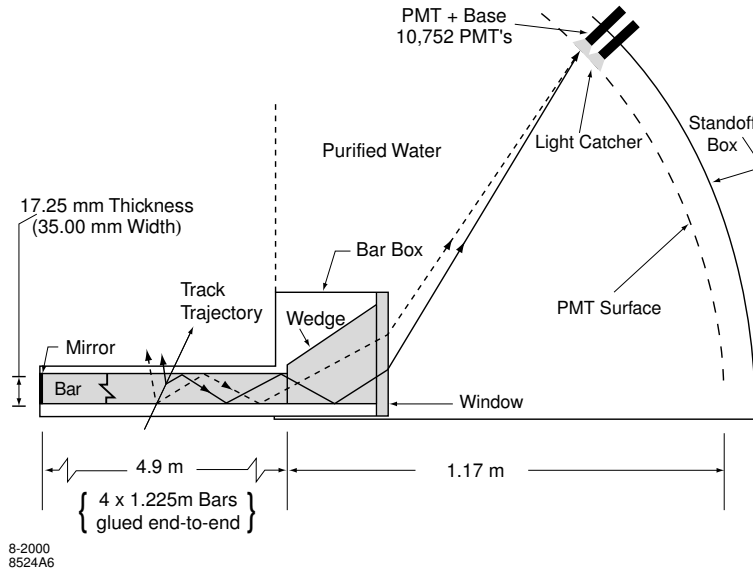


**Figure 3.7:** Overview of the DIRC. A typical path of an emitted Cherenkov photon through the DIRC is shown.

DIRC-bars are closed with mirrors to avoid losses of Cherenkov photons which are emitted in the front direction. The rear end of a bar is closed with a fused silicon *wedge*. The *wedge* with a trapezoidal profile optimizes the transition of photons between the fused silica bars and the water surface of the *standoff box*. The latter is a reservoir filled with 6 m<sup>3</sup> of purified water with a refractive index close to that of fused silica ( $n=1.346$ ). Its rear surface is instrumented with about 11,000 photomultiplier tubes which are equally distributed over the 12 sectors. Because of the boosted center-of-mass system and the resulting asymmetry of the *BABAR* detector, the DIRC photon detection system is located in the backward direction in order to minimize the material in front of the outer detector components. The DIRC possesses a thickness of 17 % radiation length at normal incidence. It covers 94 % of the azimuthal and 83 % of the polar angle.

The particle identification power of the DIRC is based on the measurement of two quantities for each track. The Cherenkov angle  $\Theta_C$  and the number of emitted Cherenkov photons are explained in the following.

### Measurement of $\Theta_C$

Cherenkov photons emitted in a DIRC-bar are focused on the photon detection surface of the *standoff box*. The focusing “pinhole” is defined by the exit aperture of the bar. The vector pointing from the center of a bar to the center of each photo multiplier tube is taken as a measure of the Cherenkov photon propagation angles. These angles and the track position information provided by the tracking devices are used to determine the Cherenkov angle  $\Theta_C$ .

In a common event with many tracks and detected Cherenkov photons,  $\Theta_C$  of a particular track is determined via a peak fit to the  $\Theta_C$  distribution of all combinations of this track with all detected Cherenkov photons. Wrong combinations of track and detected Cherenkov photon only contribute to the background of this distribution. Thus the determination of  $\Theta_C$  for a given track is possible even in presence of many wrong combinations.

### Measurement of the number of detected Cherenkov photons associated to tracks

In order to count the number of Cherenkov photons which have been emitted by a particle traversing the DIRC it is necessary to reduce wrong associations of detected Cherenkov photons to tracks. The DIRC time measurement provides information to resolve this problem. The relevant observable to distinguish between right and wrong associations is the difference between the measured and expected Cherenkov photon arrival time  $\Delta T$  [7]:

$$\Delta T = T_{\gamma,meas} - T_{\gamma,exp} \quad (3.2)$$

with

$$T_{\gamma,meas} = T_{\gamma,TDC} - T_{trig} - T_{bunch} - T_0 - T_{offset} \quad (3.3)$$

where  $T_{\gamma,TDC}$  is the arrival time of a Cherenkov photon in a photo multiplier measured in the digital chips which are part of the DIRC electronics. It is defined with respect to the DIRC trigger time  $T_{trig}$ .  $T_{bunch}$  is the incidence time of a bunch crossing.  $T_0$  is a correction which takes photo multiplier and electronic specific delays into account. The fixed number  $T_{offset}$  aligns the average of  $\Delta T$  to zero.

$$T_{\gamma,exp} = T_{TOF} + T_{\gamma,bar} + T_{\gamma,wedge} + T_{\gamma,SOB} \quad (3.4)$$

where  $T_{TOF}$  is the time-of-flight along the path from the interaction point to the middle of a DIRC-bar.  $T_{\gamma,bar}$ ,  $T_{\gamma,wedge}$  and  $T_{\gamma,SOB}$  are the propagation times of the Cherenkov photon in the DIRC-bar, -wedge and *standoff box*.

Using this information, the number of wrong associations of detected Cherenkov photons to tracks can be improved and accelerator induced background signals can be reduced by approximately a factor of 40 when  $\Delta T$  is required to be smaller than 8 ns.

## 3.4 Electromagnetic calorimeter

### 3.4.1 Purpose and layout

The purpose of the electromagnetic calorimeter (EMC) is to measure the energy, the position and the transverse shape of electromagnetic showers. It is designed to detect electrons and photons over a wide energy range of 20 MeV to 9 GeV with high resolution and efficiency. To achieve this goal the calorimeter is built from 6580 crystals. The energy deposited in such a crystal is converted into scintillation light. This light is guided to the rear end of the crystal and collected with photodiodes.

CsI(Tl) is chosen as the crystal material. The short radiation length of 1.85 cm and the small Molière radius of 3.8 cm allow a compact detector design for the measurement of fully contained showers. The emission spectrum and the high light yield allow the use of silicon photodiodes to read out the scintillation light of the crystals.

As a consequence of the boosted center-of-mass system, the EMC is asymmetric and consists of two main sections, the barrel and the endcap. A longitudinal cross-section of the EMC is shown in Figure 3.8. The cylindrical barrel with an inner radius of 91 cm and outer radius of 136 cm contains 48 rings with 120 identical crystals each. It covers the polar angle region  $26.9^\circ < \theta < 140.8^\circ$ . The conic forward endcap consists of 820 crystals in 8 rings. The coverage of the polar angle is  $15.8^\circ < \theta < 26.9^\circ$ . The crystal length in units of the radiation length differs from 17.5 in the endcap to 16.0 in the backward part of the barrel.

The properties of the crystal material, CsI(Tl), result in an excellent energy resolution:

$$\frac{\sigma_E}{E} = \frac{(2.32 \pm 0.30)\%}{\sqrt[4]{E(\text{GeV})}} \oplus (1.85 \pm 0.12)\% \quad (3.5)$$

where the terms are added in quadrature. The first term describes fluctuations in photon statistics, electronic noise and beam-generated background. The second term arises from non-uniformities in light collection, leakage in the material in front and between the crystals and uncertainties in the calibration. The angular resolution is determined by the transverse crystal size and the distance from the interaction point.

$$\sigma_\theta = \sigma_\phi = \left( \frac{3.87 \pm 0.07}{\sqrt{E(\text{GeV})}} + 0.00 \pm 0.04 \right) \text{ mrad} \quad (3.6)$$

### 3.4.2 Clusters and bumps

In general, a particle which enters the EMC and interacts with the material does not deposit its energy only in one crystal. The deposited energy is spread over several crystals. Such a group of crystals is called a “cluster”. To build clusters

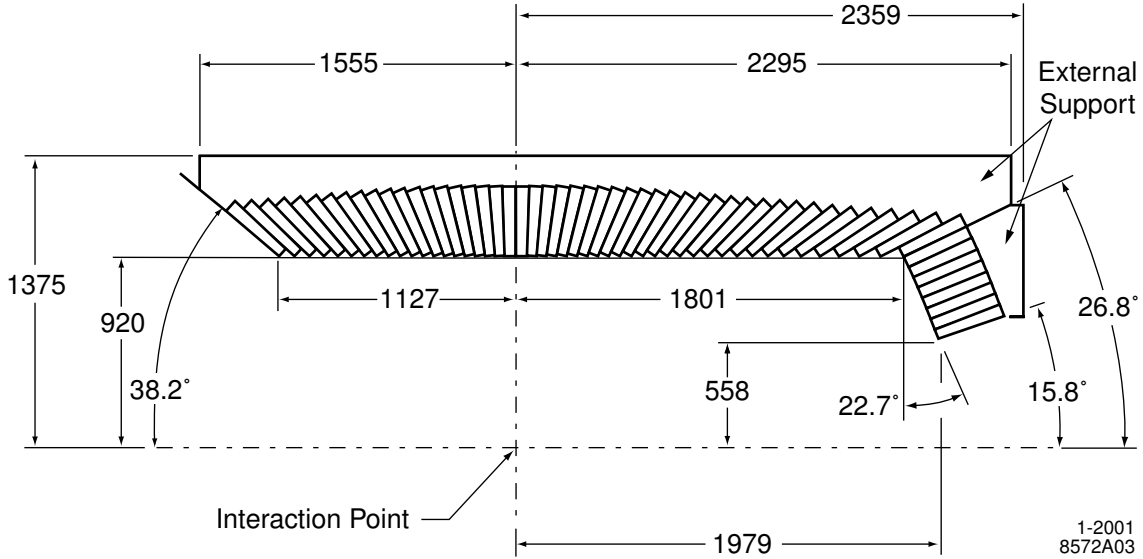


**Figure 3.8:** A longitudinal cross-section of the electromagnetic calorimeter. Only the top half is shown. (Dimensions are given in mm)

from single crystal information, the following algorithm is used. In the first step a crystal which fulfills the criterion of a measured energy larger than 5 MeV is defined as a “seed”. The second step is to add all adjacent crystals with an energy over the threshold of 1 MeV to the cluster seed. For the next neighbor crystals a minimal energy of 1 MeV and a neighboring crystal with more than 3 MeV is required. The cluster energy is defined as the sum of the energies of its associated crystals. If two particles enter the electromagnetic calorimeter close to each other and deposit energy in adjacent crystals, it is possible that the cluster has two local maxima. In this case the cluster is splitted according to the weights of its single crystal information into “bumps” with only one maximum each. The energy and the position of the “bump” are associated to one single particle.

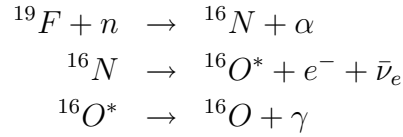
### 3.4.3 Calibration

The calibration of the EMC is performed in two steps. First the single crystal calibration is applied to assign an energy to the pulse height measured in a single crystal. It also corrects variations in the light yield from crystal to crystal and over time. The latter are mainly due to radiation damage. In a second step, the cluster corrections are applied to correct energy losses which are not due to the features of single crystals. These energy losses are due to particle interactions with material in front of the EMC and leakage between and at the end of the crystals. The measured cluster energy is too small.

### Single crystal calibration

The single crystal calibration is performed in two different energy regions with two different processes, the source calibration at 6.13 MeV and the Bhabha calibration at 3 to 9 GeV. An interpolation of the two resulting constants for each crystal provides a calibration over the whole energy range.

The source calibration is performed by pumping an irradiated fluid through aluminum pipes in front of all crystals. Photons with an energy of 6.13 MeV are emitted:



For the Bhabha calibration non-radiative Bhabha events are used.

$$e^+e^- \rightarrow e^+e^- \quad (3.7)$$

The energy deposited in the calorimeter does only depend on the polar angle  $\Theta$ . The measured deposited energy is compared with the predictions of the Monte Carlo simulation. For each crystal a calibration constant is obtained from a set of linear equations which relate the measured and the predicted energy.

### Cluster corrections

Two cluster correction methods are used to correct energy losses. The first correction is the so called  $\pi^0$  *calibration*. It is used for photons with an energy in the range from 0.03 GeV to 2 GeV. The  $\pi^0$ -meson decays into two photons. The following relation is used to extract correction functions.

$$m_{\pi^0} = \sqrt{2E_{\gamma,1}E_{\gamma,2}(1 - \cos \alpha)} = 135.0 \text{ MeV} \quad (3.8)$$

where  $E_{\gamma,1,2}$  are the photon energies and  $\alpha$  is the angle between the photon trajectories. The second correction, the Monte Carlo correction, uses simulated single photon events. The simulated cluster energy  $E_{raw}$  is compared with the generator level energy  $E_{true}$  depending on the energy and the polar angle.

$$\frac{E_{raw}}{E_{true}} = f(E, \cos \Theta) \quad (3.9)$$

This function is used to correct energies above 2 GeV, since this energy range is not covered by the  $\pi^0$  *calibration*.

### 3.4.4 Material in front of the EMC

The energy resolution of the electromagnetic calorimeter is affected by the interaction of particles with the material in front of the EMC. Figure 3.9 shows the distribution of the material in front of each component of the *BABAR* detector in units of radiation length. The DIRC material corresponds to 17 % to 30 % of a radiation length depending on the polar angle. This is the largest contribution to the amount of material a particle traverses before it reaches the EMC. In this

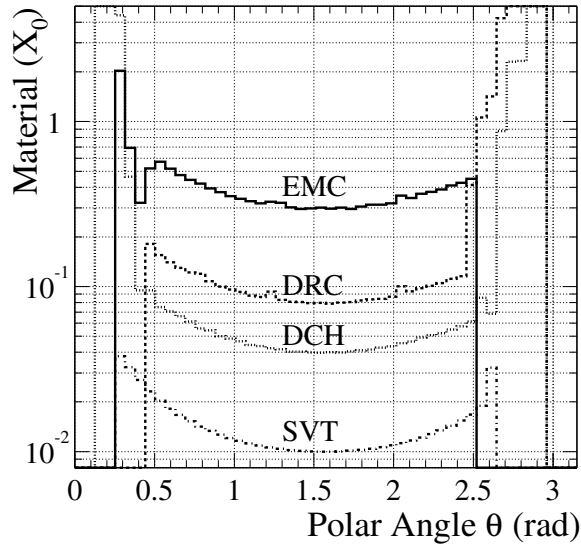


**Figure 3.9:** Amount of material in units of radiation length  $X_0$  a particle traverses before it reaches a specific detector component

study the approach will be presented to improve the energy resolution using the DIRC to detect photons which started to shower in front of the calorimeter.

## 3.5 Simulation and data sample

### Monte Carlo simulation

The Monte Carlo simulation of the *BABAR* detector uses *EvtGen* [8] which is an event generator designed for the simulation of physics of B-meson decays. In particular, *EvtGen* provides a framework to handle complex sequential decays and CP violating decays. The detector setup is simulated with *Geant4* [9] which is a framework for the simulation of the passage of particles through matter.

Background events are collected during normal data acquisition. These background events are random triggers that contain no physics data, but only machine background and detector noise. They are overlaid to the generated Monte Carlo

data. This procedure gives an optimal description of backgrounds and accounts for the changes in the beam and detector conditions over time.

The Monte Carlo data sample used in this study is a generic  $B^0\bar{B}^0$  Monte Carlo. It represents a mixture of neutral B-meson decays. The relative branching fractions correspond to the measured and expected neutral B-meson decays as published by the PDG. The sample contains 1,190,000 events.

Furthermore, a second Monte Carlo sample without an overlaid background is used. It consists of single photon events. This sample is chosen, since an unbiased sample is necessary for the study of photons which started to shower in front of the calorimeter. The number of used events varies depending on the considered problem. In the following chapters this number is given when simulated single photons are used.

### **Data**

The used data sample contains a fraction of the data collected during the fourth data taking period (Run 4) of the *BABAR* detector. The sample contains 1,290,000 events which corresponds to a luminosity of 73.2 1/pb collected in march, april and may of 2004. In order to minimize a possible bias in the underlying event sample, no further selection criteria have been applied.



# Chapter 4

## Preshower detection with the DIRC

The aim of this study is the improvement of the photon energy resolution which is degraded by the interaction of photons and electrons with material of the inner components of the *BABAR* detector. A fraction of these particles starts electromagnetic showers before they reach the EMC. This causes losses in the measured energy of calorimeter clusters. Since the energy of electrons is measured indirectly in the tracking devices of the *BABAR* detector, electrons are not considered in this study. For photons, the average energy scale is determined correctly by the application of the  $\pi^0$  calibration. The latter also accounts for the average energy losses due to preshowers. However, the existence of “preshowers” leads to a degradation of the energy resolution. If a particle starts to shower before it has reached the calorimeter, the part of the shower which is in front of the calorimeter is called a “preshower”. Thus, it is interesting to identify preshowers. This chapter first discusses the identification of preshowers. The approach to use the DIRC as a preshower detector is presented. The photons which started to shower in front of the EMC are identified by the association of Cherenkov photons detected in the DIRC. Cherenkov photons are emitted in the DIRC quartz bars by initial  $e^+e^-$ -pairs in the electromagnetic shower.

### 4.1 Photon showers

The first step to analyze the impact of preshowers on the photon energy resolution is to verify how much preshowers actually degrade the energy resolution. For this purpose Monte Carlo simulations are used. Single photon events are generated to study an unbiased event sample. The simulation provides the starting point of an electromagnetic shower on generator level. The radial part  $R$  of the starting point is used to decide if a cluster started to shower in front of the EMC. This leads to the following definition of two photon samples to indicate whether a photon

started showering before the EMC or not:

$$\begin{aligned} \text{generated w/o preshower} : R &=> R_{EMC} \\ \text{generated w/ preshower} : R &< R_{EMC}, \end{aligned} \quad (4.1)$$

where  $R_{EMC} = 91$  cm is the inner radius of the electromagnetic calorimeter.

The energy loss  $\Delta E$  due to preshowers is shown in Figure 4.1.

$$\Delta E = E_{true} - E \quad (4.2)$$

where  $E$  is the cluster energy. The cluster corrections are not yet applied.  $E_{true}$  is the energy of the generated particle.

The energy distribution for *generated-w/o-preshower* photons is compared with the *generated-w/-preshower* distribution. The mean value of the latter is clearly shifted to higher  $\Delta E$  values and the distribution is more asymmetric. Since the only difference between the two distribution is the starting point of the shower, the difference in the shapes can only be explained with the energy lost in the preshower.

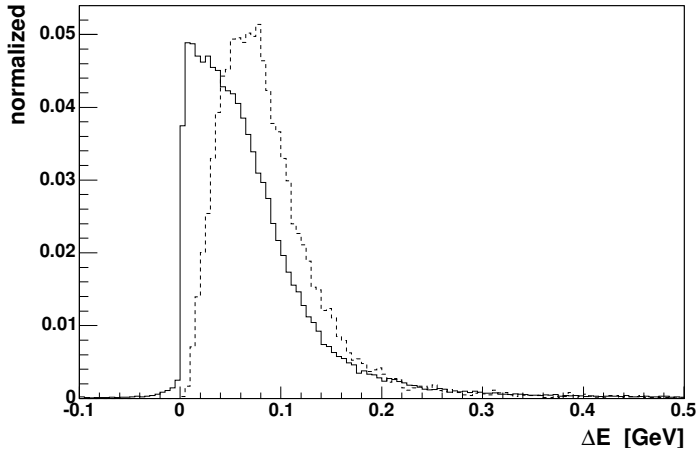


**Figure 4.1:** *Simulated single photon events: The energy loss  $\Delta E$  for photons with the starting point of showers in the EMC (solid line) is compared with  $\Delta E$  for photons with the starting point in front of the calorimeter (dashed line). The latter distribution is shifted to higher values.*

The second step is to determine the number of photons which started to shower in front of the EMC. Figure 4.2 shows the distribution of  $R$  in the detector. This study is restricted to the barrel part of the EMC, that means,  $0.473 \text{ rad} < \theta < 2.456 \text{ rad}$ . One can easily see that the majority of preshowers (12 %) starts in the DIRC.

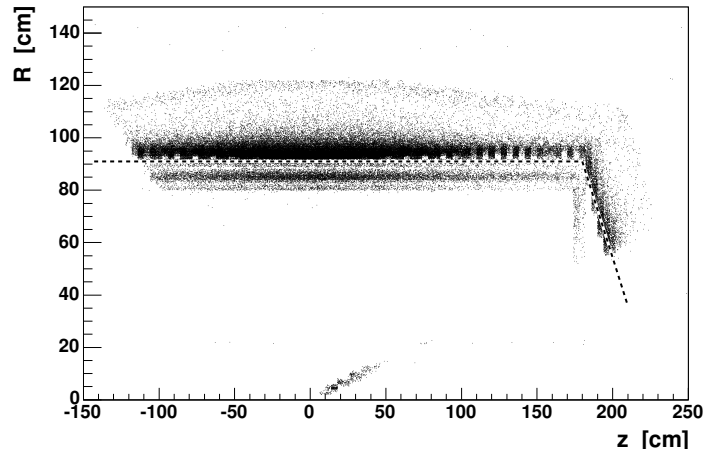


**Figure 4.2:** *Simulated single photon events: Radial part  $R$  of the starting point of a preshower versus the  $z$ -coordinate of a photon cluster. The dashed line indicates the EMC.*

Sub-Detector	Inner Radius	$N_{\text{shower}}$
SVT		0.02 %
DCH	23.60 cm	0.96 %
DIRC	81.71 cm	12 %
EMC	91.00 cm	87 %

**Table 4.1:** *Fraction of photons  $N_{\text{shower}}$  which started to shower in a certain sub-detector obtained from the generator information (Monte Carlo simulation).  $\theta$  is restricted to the interval  $[0.473, 2.456]$  rad.*

Table 4.1 shows the fractions of photons where the shower started in the sub-detectors. 13% of the photons start to shower in front of the EMC.

This shows that preshowers degrade the resolution of the photon energy reconstruction and that the number of photons which showered in front of the calorimeter, in particular in the DIRC, is significant. This leads to the fundamental idea for this thesis. The energy resolution might be improvable by rejection clusters with preshowers. Since the shower starts with a pair of electron and positron, emitting Cherenkov light, the DIRC itself can be used to detect preshowers. It will be shown, that the association of detected Cherenkov photons to clusters is possible and can be used to detect preshowers.

## 4.2 Cherenkov photons and calorimeter clusters

In order to associate detected Cherenkov photons to a particle traversing a quartz-bar and to measure the Cherenkov angle  $\Theta_C$  it is necessary to know the point where the particle hits the DIRC and the entrance angle of the trajectory. In case of charged particles, this trajectory is given by the reconstructed track measured in the tracking devices of the *BABAR* detector. For neutral particles, this trajectory is defined in this thesis as a straight line from the beam spot to the centroid of the cluster.

Before one can try to associate detected Cherenkov photons in multi-particle events, it is necessary to study the properties of Cherenkov light emitted by multiple charged particles in a shower. The resolution of  $\Theta_C$  and  $\Delta T$  might be very different from what is measured for a single charged particle traversing the DIRC. Single photon Monte Carlo simulations allow to study these properties without the need of a working association between Cherenkov photons and clusters. It is simply assumed, that all detected Cherenkov photons originate from the single simulated photon. The single photon Monte Carlo has been produced especially for this study without overlaid backgrounds from real data. Figure 4.3 shows the distribution of  $\Theta_C$  and  $\Delta T$  for single photon Monte Carlo events. The distributions of both quantities have a peak at the expected values. The expected Cherenkov angle is  $\Theta_{C,exp} = 0.82$  rad for particles with  $\beta = 1$ , i.e. electrons in the shower. The difference between the measured and expected arrival time of a Cherenkov photon should be close to zero ( $\Delta T_{exp} = 0$ ).

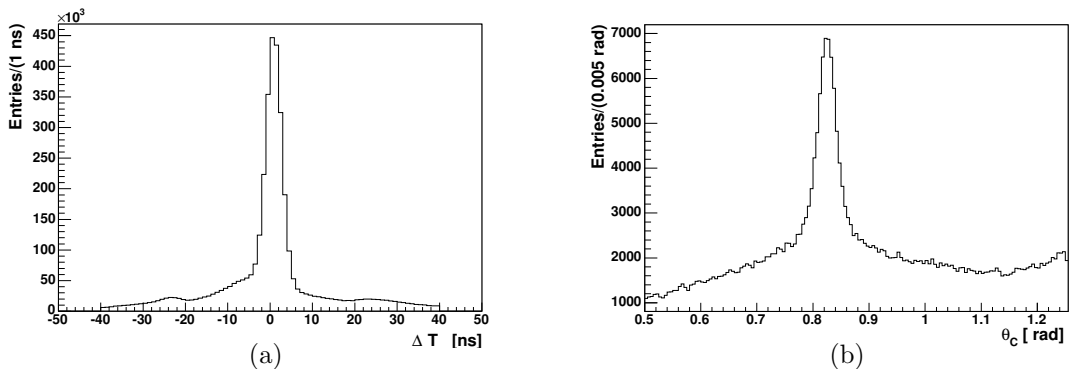


**Figure 4.3:** *Simulated single photon events: (a)  $\Delta T$  distribution and (b)  $\Theta_C$  distribution.*

A clear peak of the  $\Theta_C$  distribution was not necessarily expected, since the charged particles in an electromagnetic shower might differ slightly in direction with the neutral particle which induced the shower. Due to the clear peak, Cherenkov photons detected at the rear surface of the *standoff box* should form

ring segments. Figure 4.4 shows the number of detected Cherenkov photons as a function of the x- and y-coordinate of the photo multipliers in the *standoff box* of the DIRC. 2000 simulated single photon events were generated with an energy of 500 MeV and entered the DIRC at a fixed polar angle  $\theta=-0.74$  rad and azimuthal angle  $\phi=-1.85$  rad. Some of the photons started to shower in the DIRC. The detected Cherenkov photons emitted by the electrons and positrons

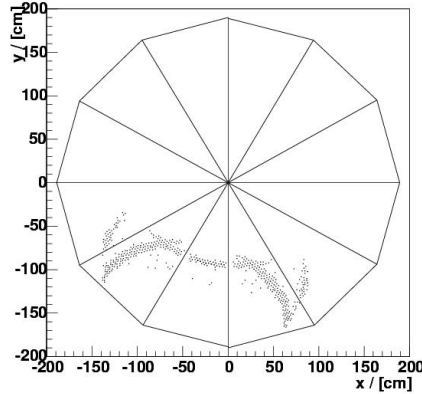


**Figure 4.4:** *Event display of the DIRC. 2000 single photons with an energy of 500 MeV were simulated in the backward region of the DIRC. The detected Cherenkov photons form ring segments.*

in the electromagnetic shower appear as ring segments in the *standoff box*. This is a further verification that the association of detected Cherenkov photons to photon clusters is feasible.

The next step is to test whether the reconstruction of the Cherenkov angle  $\Theta_C$  depends on the entrance position of photons in DIRC-bars. In order to test such a possible dependence the polar angle  $\theta$  as well as the azimuth angle  $\phi$  of a photon clusters are considered. The polar angle coordinate  $\theta$  is divided in five equidistant intervals ( [25.6,48.7], [47.7, 71.9], [71.9,95.1], [95.1,118.3], [118.3,141.5]). Figure 4.5 shows the binning in  $\theta$  and  $\phi$ . Only the barrel region of the calorimeter is considered, since this part is covered by the DIRC. Furthermore, the following division is applied in each  $\theta$  bin. Each *bar-box* is divided in four  $\phi$  bins, which also can be seen in Figure 4.5. The first bin, 0 to 0.83, degree covers the gap between the *bar boxes* of the DIRC. The other bins are 0.83 to 5 degree, 5 to 10 degree and 10 to 15 degree.

The assumption is made that the reconstruction of the Cherenkov angle is independent from the *bar-box* traversed by the photon. Since, each *bar-box* covers 30 degrees of the azimuth angle, all *bar-boxes* are projected on the  $\phi$  interval from 0 to 30 degrees, and further, since a *bar-boxes* is symmetric, on the interval from 0 to 15 degrees.

Figure 4.6 shows the  $\Theta_C$  distribution in the intervals described above. The position of the peak is located at the expected value  $\Theta_{C,exp} = 0.82$  rad. Hence the reconstruction of the Cherenkov angle is independent of angular binning. However, the background varies significantly.

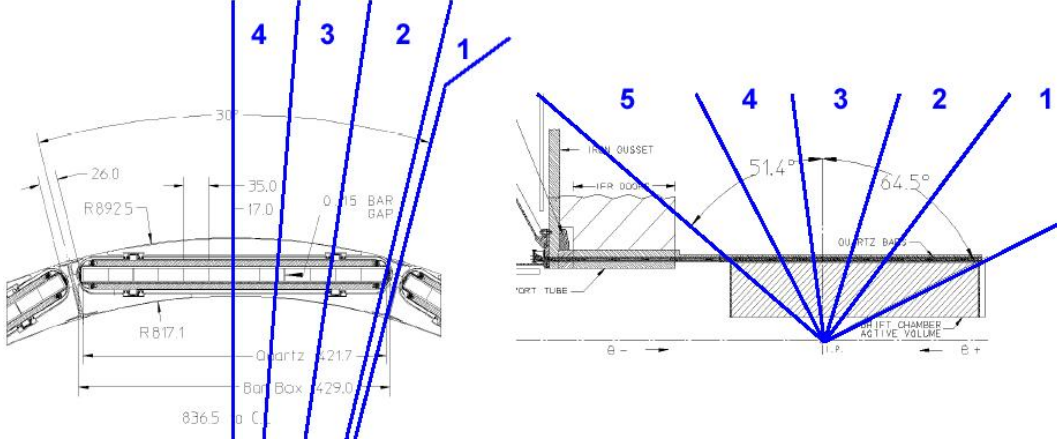


**Figure 4.5:** A schematic overview of the angular binning applied for the histograms shown in Figure 4.6. (left)  $\phi$ : All 24 DIRC-sector halves are projected on the azimuth angle interval from 0 to 15 degrees. (right)  $\theta$ : The polar angle region is divided in five equidistant bins.

Single photon Monte Carlo can also be used to verify the correlation between the energy loss  $\Delta E = E_{raw} - E_{true}$  and the number of detected Cherenkov photons. In Figure 4.7, the energy loss  $\Delta E$  is plotted versus the number of detected Cherenkov photons in case of simulated single photon events. A clear correlation is visible. The energy loss increases with an increasing number of detected Cherenkov photons. Hence, the number of detected Cherenkov photons allows to decide whether a photons started to shower in front of the EMC. Further, this number is a measure for the energy loss.

Up to this point, the missing information of the actual path the Cherenkov photon had taken from the cluster to the photo multiplier tube has been ignored. For each detected Cherenkov photon all possible path, with their respective values for  $\Theta_C$  and  $\Delta T$  have been used. The ambiguity in this calculation has been described in Section 3.3. Such a possible path between detected Cherenkov photons and clusters is called a DIRC-solution in the following.

In the case of events with several clusters, the association of detected Cherenkov photons to photon clusters is also ambiguous. Detected Cherenkov photons can be associated to more than one cluster per event. This problem needs to be resolved, since the number of associated Cherenkov photons is intended to be the crucial criterion to decide whether a photon started to shower in front of the EMC or not. The major problem is the unique association of Cherenkov

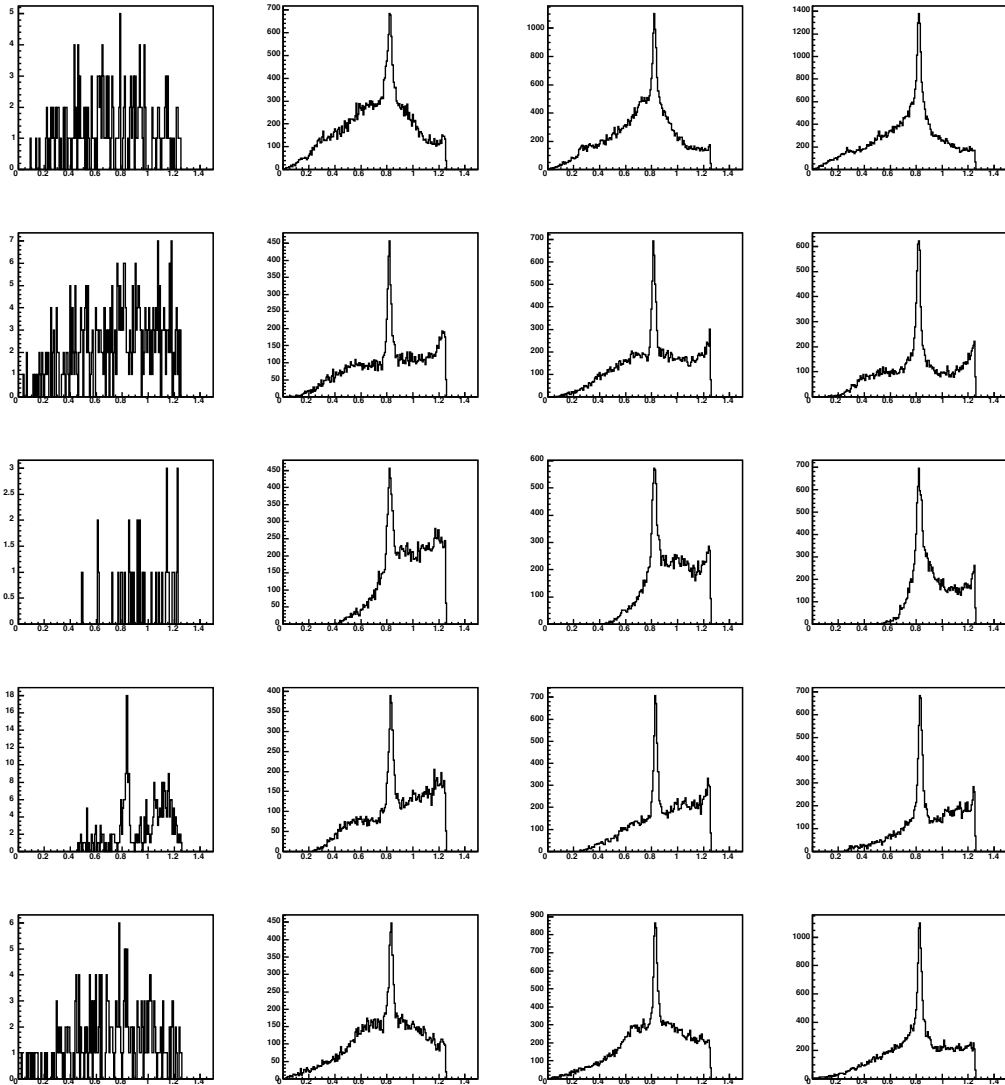


**Figure 4.6:** Cherenkov angle  $\Theta_C$  distribution for simulated single photon events:

From left to right: azimuthal angle  $\phi$  bins.

From top to bottom: polar angle  $\theta$  bins.

The first column, i.e., the first  $\phi$  bin, corresponds to the gap between the bar boxes of the DIRC. It is expected that only a few DIRC-hits are found in this interval.

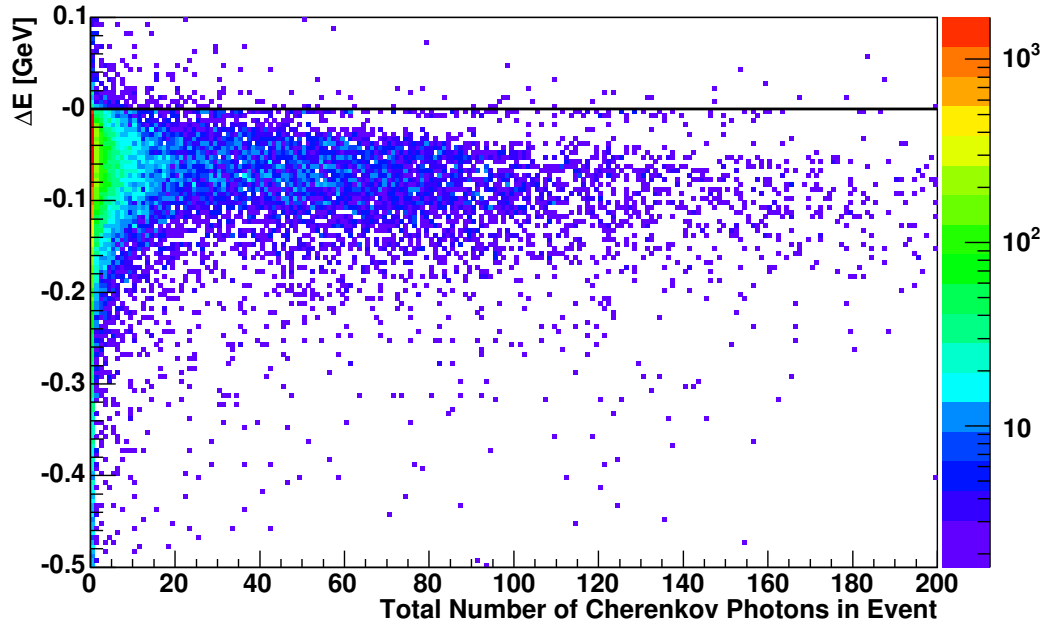


**Figure 4.7:** The energy loss  $\Delta E$  is plotted versus the number of Cherenkov photons. A clear correlation is visible.

photons to clusters. Figure 4.8 shows the number of clusters, the number of detected Cherenkov photons, and the number of DIRC-solution per event in case of generic  $B^0\bar{B}^0$  Monte Carlo simulations. It is clearly visible that the number of DIRC-solutions is much larger than the number of detected Cherenkov photons. On average, there are about 22 DIRC-solutions per detected Cherenkov photon.

A further step is to study the  $\Theta_C$  and  $\Delta T$  distribution for generic  $B^0\bar{B}^0$  Monte Carlo (Figure 4.9). In this case the wrong association of detected Cherenkov photons is obvious. Both distributions are dominated by the background. Thus, the ambiguities of the association of detected Cherenkov photons to photon clusters in ordinary events with more than one particle traversing a DIRC-bar need to be resolved. The solution of this problem is crucial to the correct identification of preshowers and is, hence, the topic of the next sections.

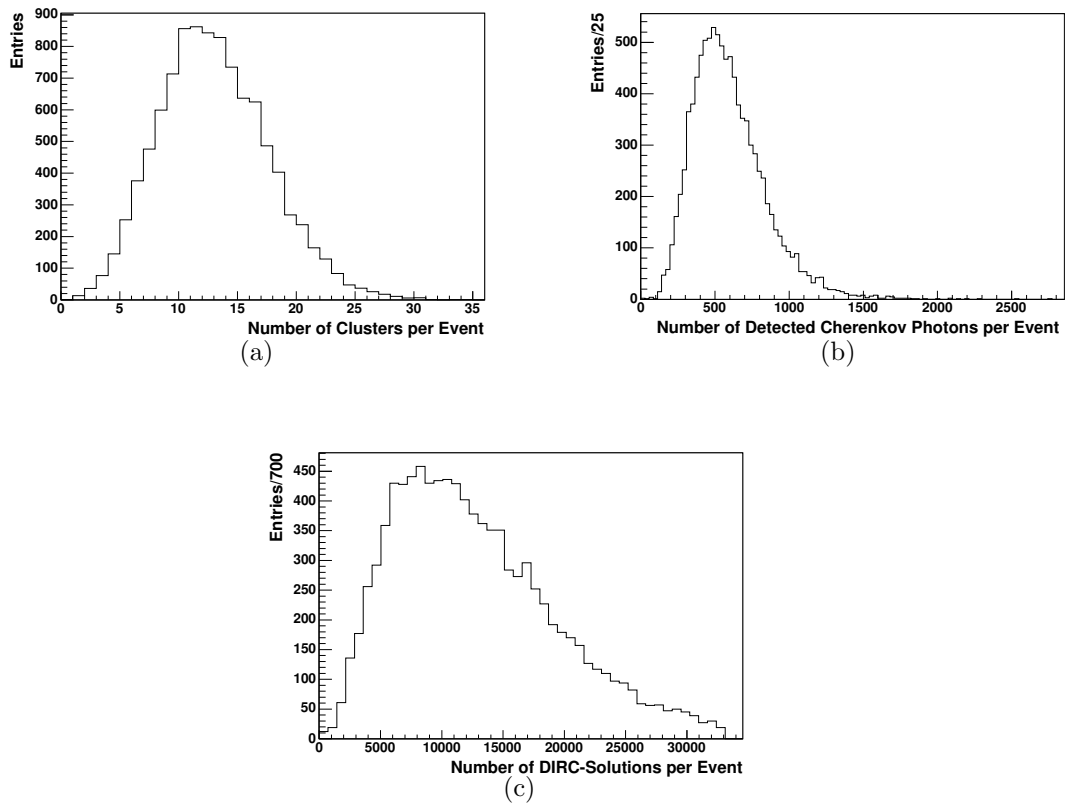


**Figure 4.8:** Generic  $B^0\bar{B}^0$  Monte Carlo simulation: **(a)** Number of clusters per event. The mean value is twelve. **(b)** Number of detected Cherenkov photons per event. On average, there are almost 600 photo multiplier signals per event. **(c)** Number of DIRC-solutions per event. The mean value is about 13,000.

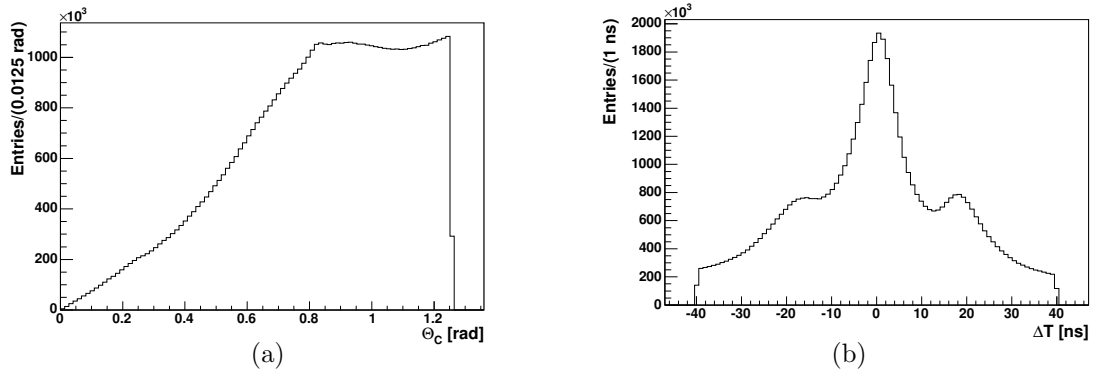


**Figure 4.9:** (a)  $\Theta_C$  and (b)  $\delta T$  distribution for generic  $B^0\bar{B}^0$  Monte Carlo events. The distributions are dominated by wrong associations of detected Cherenkov photons to photon clusters.

### 4.3 Selection of clusters

In the last section it was shown in single photon Monte Carlo, that there is a clear correlation between the total number of Cherenkov photons and the energy loss  $\Delta E$ . Looking into Monte Carlo simulations of full  $B^0\bar{B}^0$  events with multiple neutral and charged particles, it has also been seen that the correct association of Cherenkov photons to photon clusters is crucial. Before focusing on this difficult association, the restriction is made in this thesis to clusters where one can expect the association to yield the best results.

The cluster energy  $E_{raw}$  is required to be larger than 100 MeV to suppress beam background photons. It is evident, that the association will perform best on isolated clusters. Thus, no second cluster is allowed to be within an angle of 15 degrees with respect to the cluster under study. This choice is motivated by the dimensions of a DIRC-*bar box*. Each *bar box* covers an azimuthal angle of 30 degrees. The distance to the next charged track needs to be larger than 30 cm. Both requirements together result in the selection of clusters which are isolated from other objects which might emit Cherenkov photons. The selection criteria reduce the mean number of clusters per event from 12 to 4 in the generic  $B^0\bar{B}^0$  Monte Carlo sample (see Figure 4.10).

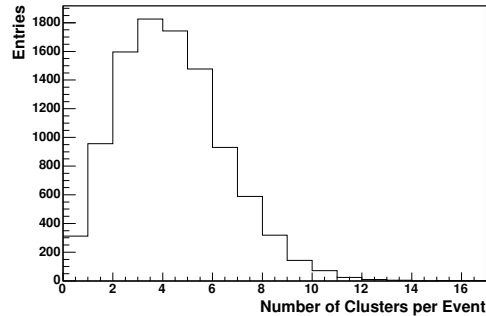


**Figure 4.10:** *Number of clusters per event after the application of the selection. The mean value is 4.*

## 4.4 Selection of detected Cherenkov photons

In Section 4.2 the DIRC-solution was introduced. This term describes all possible paths between a detected Cherenkov photon and the charged particle in the shower which emitted the Cherenkov light. Each detected Cherenkov photon has several DIRC-solutions. However, only one solution needs to be found for each Cherenkov photon in order to assign it to the right photon cluster. In the following, the steps which are required to select the *best solution* for each DIRC-hit are described. Generic  $B^0\bar{B}^0$  Monte Carlo is considered.

Cherenkov photons associated to charged tracks are discarded. For the remaining detected Cherenkov photons all possible DIRC-solutions are considered. The quantities  $\Delta T$  and  $\Theta_C$  which characterize each DIRC-solution are used to find the *best solution*.

A rather loose pre-selection of  $\Delta T < 40$  ns is required to reduce combinatoric background.

For each of the remaining DIRC-solutions the quantity  $A$  is defined as a function of  $\Delta T$  and  $\Theta_C$ :

$$A = A(\Delta T, \Theta_C) = \left( \frac{\Delta T - \Delta T_{exp}}{8\text{ns}} \right)^2 + \left( \frac{\Theta_C - \Theta_{C,exp}}{0.05\text{rad}} \right)^2 \quad (4.3)$$

where  $\Theta_{C,exp} = 0.82$  rad is the expected Cherenkov angle and  $\Delta T_{exp} = 0$  ns the expected difference between the measured and expected arrival time of a Cherenkov photon. The normalization values 8 ns and 0.05 rad correspond to the width of the peak in the  $\Delta T$  and  $\Theta_C$  distribution for simulated single photon events (Figure 4.3).

Values of  $\Delta T$  and  $\Theta_C$  close to the expectation result in a small value of  $A$ . The definition of  $A$  allows a selection of DIRC-solutions in “circles” in the  $(\Delta T - \theta_C)$  plane (Figure 4.11). Each  $\Delta T$  and  $\Theta_C$  pair is represented by a point in this plane. The expected values of these quantities describe the center of a circle with the radius  $A$ .

The *best solution* for each detected Cherenkov photon is the solution with the smallest value of  $A$ . The detected Cherenkov photon is assigned to only one cluster in the event. Thus, the detected Cherenkov photon is characterized by the  $\Delta T$  and  $\Theta_C$  values of the *best solution*.

Figure 4.12 and Figure 4.13 show the resulting  $\Theta_C$  and  $\Delta T$  distributions for the detected Cherenkov photons associated to clusters. The histograms shown are normalized to unity which allows to compare the shape of the distributions for data and generic  $B^0\bar{B}^0$  Monte Carlo. The  $\Theta_C$  distributions show a good agreement but the  $\Delta T$  resolution is clearly sharper in the Monte Carlo simulation. For the scope of this thesis the agreement is acceptable. Further investigations might be necessary later on. The slight shoulders in the distribution at  $\pm 20$  ns are due to the forward-backward ambiguity in the reconstruction of the Cherenkov photon. This ambiguity will be resolved by the selection described in Section 4.5.1.

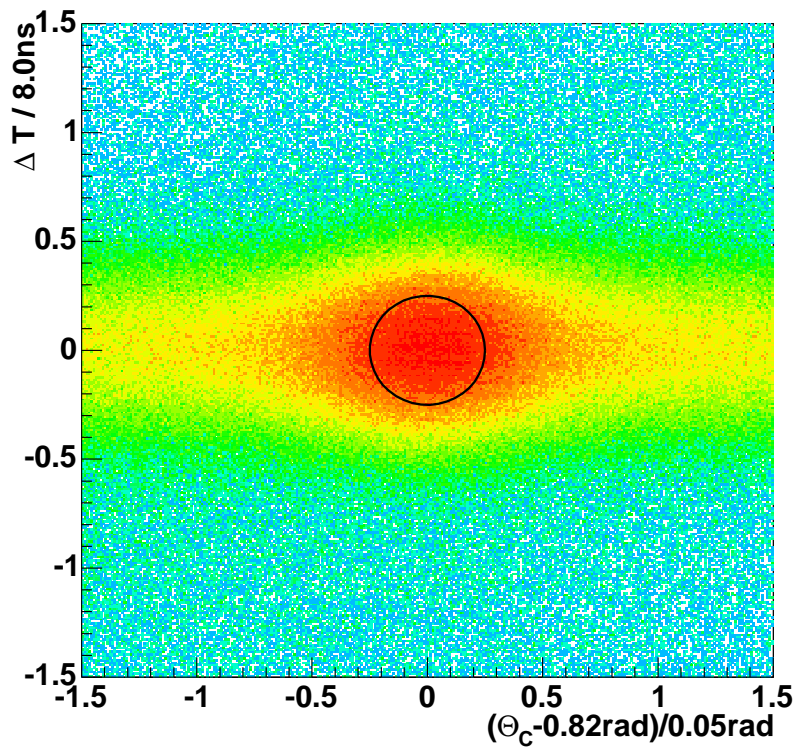


**Figure 4.11:** *The  $\Delta T$  and  $\Theta_C$  values of DIRC-solutions of simulated single photon events. The normalization with 8 ns and 0.05 rad simplifies the selection to be representable as circle. As an example a selection requirement of  $A(\Theta_C, \Delta T) < 0.25$  is shown as a circle.*

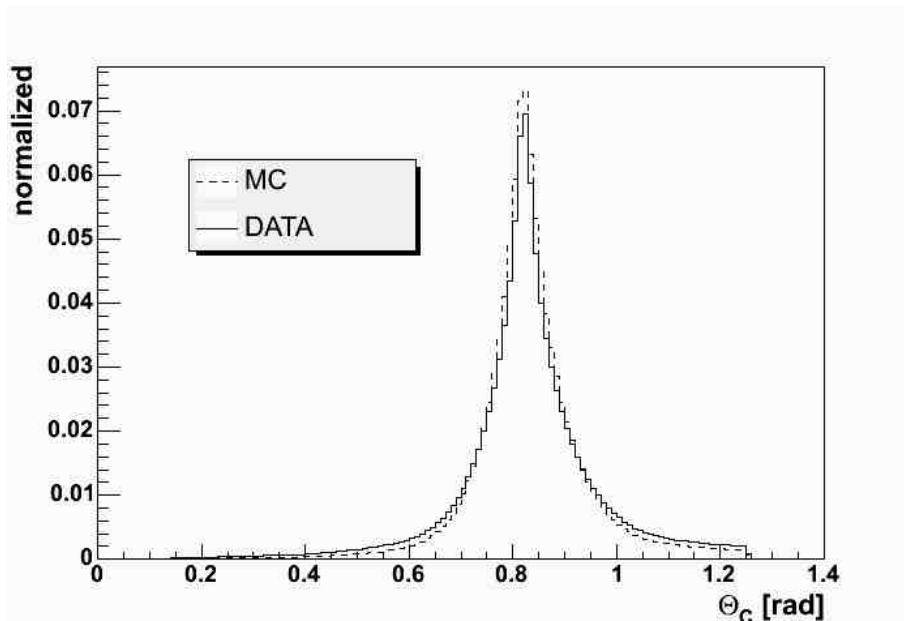


**Figure 4.12:** Cherenkov angle  $\Theta_C$ . The Monte Carlo simulation (dashed) as well as the data (solid) distribution peak at the expected value  $\Theta_{C,exp} = 0.82$  rad.

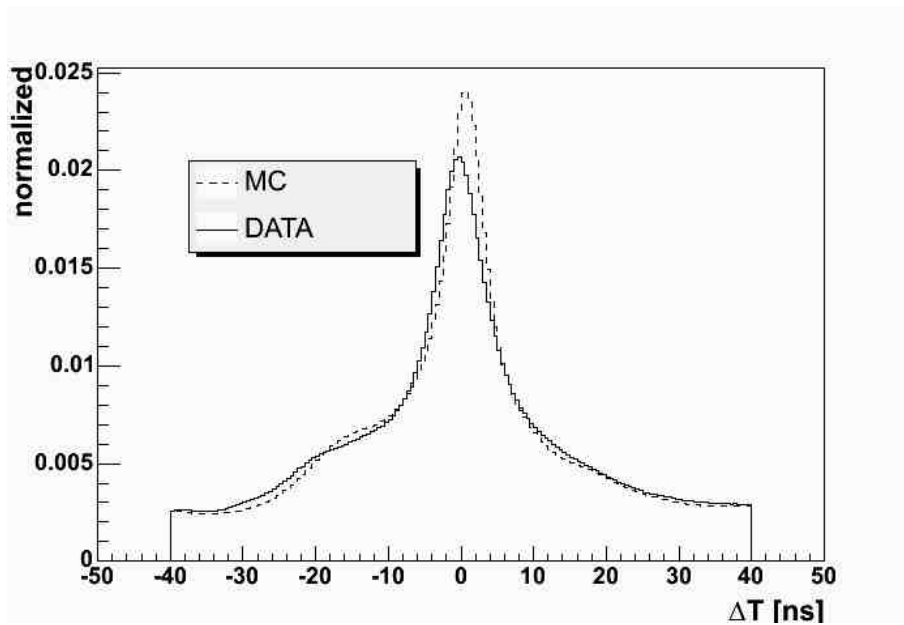


**Figure 4.13:** Difference between the measured and expected arrival time  $\Delta T$  of a photon detected in the DIRC. The Monte Carlo distribution is shown as a dashed line, the data as a solid line.

However, the comparison with a  $\Delta T$  and  $\Theta_C$  distribution before the association process (Figure 4.3) shows that the background of ambiguities is much reduced.

## 4.5 Identification of preshowers

### 4.5.1 Definition of detected preshowers

In the last section, the *best solution* for each detected photon was determined. However, the *best solution* might still be not a “good” solution. A further selection is required to allow an satisfactory identification of preshowers. The selection is based on two parameters which are defined in the following.

The first selection parameter is  $A_{max}$ . This number describes the maximum value for the quantity  $A(\delta T, \Theta_C)$  which is defined in Equation 4.3.

$$A(\delta T, \Theta_C) < A_{max} \quad (4.4)$$

Detected Cherenkov photons which do not satisfy this requirement are discarded. The number of remaining detected Cherenkov photos is  $N_C$ . Based on the information from the DIRC, two samples of photon clusters are defined. These samples are called the *detected-w/o-preshower* or *detected-w/-preshower* sample to indicate whether the photon is believed to have showered in front of the EMC or not.

The two samples are defined as follows:

$$\begin{aligned} \textit{detected-w/o-preshower} : N_C &\leq N_{max} \\ \textit{detected-w/-preshower} : N_C &> N_{max} \end{aligned} \quad (4.5)$$

where  $N_{max}$  is the maximum number of detected Cherenkov photons assigned to a photon which is believed to have reached the EMC without starting a preshower. The two parameters  $N_{max}$  and  $A_{max}$  are correlated. If  $A$  is smaller, there are less detected Cherenkov photons assigned to a photon cluster. Hence, photons which start to shower in front of the EMC need a smaller number of associated DIRC-hits to be identified correctly.

Both numbers  $N_{max}$  and  $A_{max}$  are subject to optimization: They are varied in order to achieve the best possible assignment of clusters to one of the two *detected* samples. This optimization procedure is described in Section 4.5.3. The quantities which are maximized, i.e., efficiency and pollution, are defined in the next section.

### 4.5.2 Definition of efficiency and pollution

Before the optimization starts, efficiency and pollution, the two quantities which quantify the quality of the selection will be defined.

The identification efficiency and the pollution of photons which started to shower in front of the electromagnetic calorimeter are defined using the generator level information provided by the Monte Carlo simulation. The efficiency for

the correct assignment of a photons which did not shower in front of the EMC (*generated-w/o-preshower*) to the *detected-w/o-preshower* sample is defined as:

$$\epsilon_{woP} = \frac{N(\textit{detected-w/o-preshower} \ \& \ \textit{generated-w/o-preshower})}{N(\textit{generated-w/o-preshower})} \quad (4.6)$$

where N denotes the number of photon clusters assigned to a certain photon set. For example,  $N(\textit{detected-w/o-preshower} \ \& \ \textit{generated-w/o-preshower})$  is the number of clusters assigned to the *detected-w/o-preshower* sample as well as to the *generated-w/o-preshower* sample. The subscript *woP* of the efficiency stands for *without preshower*.

The efficiency for the correct assignment of photons which did shower in front of the EMC is then:

$$\epsilon_{wP} = \frac{N(\textit{detected-w/-preshower} \ \& \ \textit{generated-w/-preshower})}{N(\textit{generated-w/-preshower})} \quad (4.7)$$

The pollution specifies the fraction of photons which have been misidentified with respect to the generator level Monte Carlo information, that means  $P_{woP}$  describes the number of clusters which started to shower in front of the EMC (*generated-w/-preshower*) and were assigned to the *detected-w/o-preshower* sample.

$$P_{woP} = \frac{N(\textit{detected-w/o-preshower} \ \& \ \textit{generated-w/-preshower})}{N(\textit{detected-w/o-preshower})} \quad (4.8)$$

A corresponding pollution of the sample of photons which have been identified as preshowers is then:

$$P_{wP} = \frac{N(\textit{detected-w/-preshower} \ \& \ \textit{generated-w/o-preshower})}{N(\textit{detected-w/-preshower})} \quad (4.9)$$

Note, by definition the efficiency and the pollution for one of the two samples do not add to one. The optimization process described in the next section tries to find the optimal relation between the identification efficiency and the pollution of a sample.

### 4.5.3 Optimization of the preshower detection

The parameters  $N_{max}$  and  $A_{max}$  need to be optimized in order to identify the photons which showered in front of the EMC with high efficiency and lowest pollution. In order to maximize the efficiency and at the same time to minimize the pollution it was decided to maximize the following variable M which combines the values for efficiency and pollution:

$$M = \epsilon_{wP} \cdot (S_{woP} - P_{wP}) \cdot \epsilon_{woP} \cdot (S_{wP} - P_{woP}) \quad (4.10)$$

The numbers  $S_{woP}$  and  $S_{wP}$  are the fractions of photon contained in *generated-w/o-preshower* and the *generated-w/-preshower* sample respectively. One finds  $S_C = 0.87$  and  $S_D = 0.13$ . The term  $S - P$  is increasing with a decreasing pollution. It is multiplied with the efficiency in order to account for the magnitude of the value of the efficiency. The choice of  $M$  follows the assumption that the highest possible pollution corresponds to a random association of clusters to the *detected* samples. In this worst case the fraction of *generated-w/-preshower* photons would be the same in both *detected* samples. Both samples would contain 13% of *generated-w/o-preshower* photons and 87% of *generated-w/o-preshower* photons. Hence the highest possible pollution of the *detected-w/o-preshower* is 13% and the highest possible pollution of the *detected-w/-preshower* is 87%.

The value of  $M$  is calculated for each parameter pair  $A_{max}$  and  $N_{max}$ . The parameter  $A_{max}$  is varied in the interval between 0.05 and 0.45 in steps of 0.05.  $N_{max}$  runs through the values 3 to 11.

Figure 4.14 and Figure 4.15 show the efficiency and the pollution for both *detected* samples obtained for a certain pair of parameter values. The different markers denote the varied parameter  $A_{max}$ . On the x-axis the parameter  $N_{max}$  is plotted. In case of the *detected-w/o-preshower* sample both quantities increase towards higher  $N_{max}$  and higher  $A_{max}$ . For the *detected-w/-preshower* sample the opposite effect is visible.

The obtained values of  $M$  for each parameter set are shown in Table 4.2.

M	$A_{max}$									
		0.05	0.10	0.15	0.20	0.25	0.30	0.35	0.40	0.45
$N_{max}$	3	0.005	0.010	0.011	0.011	0.011	0.011	0.010	0.009	0.009
	4	0.003	0.008	0.010	0.011	<b>0.012</b>	0.011	0.011	0.011	0.010
	5	0.002	0.006	0.009	0.011	0.011	0.011	0.011	0.011	0.011
	6	0.001	0.005	0.008	0.009	0.010	0.011	0.011	0.011	0.011
	7	0.001	0.004	0.006	0.008	0.009	0.010	0.010	0.011	0.011
	8	.000	0.003	0.005	0.007	0.008	0.009	0.010	0.010	0.010
	9	0.000	0.002	0.004	0.006	0.007	0.008	0.009	0.009	0.009
	10	0.000	0.001	0.003	0.005	0.006	0.007	0.008	0.008	0.009
	11	0.000	0.001	0.002	0.004	0.005	0.006	0.007	0.007	0.008

**Table 4.2:**  $M$  obtained for a certain optimization parameter set. The maximum value is 0.012 for  $N_{max}=4$  and  $A_{max}=0.25$ .

The maximum  $M$  is 0.012. Thus, the optimal parameters found in the optimization process are

$$\begin{aligned} N_{max} &= 4 \\ A_{max} &= 0.25 \end{aligned} \tag{4.11}$$

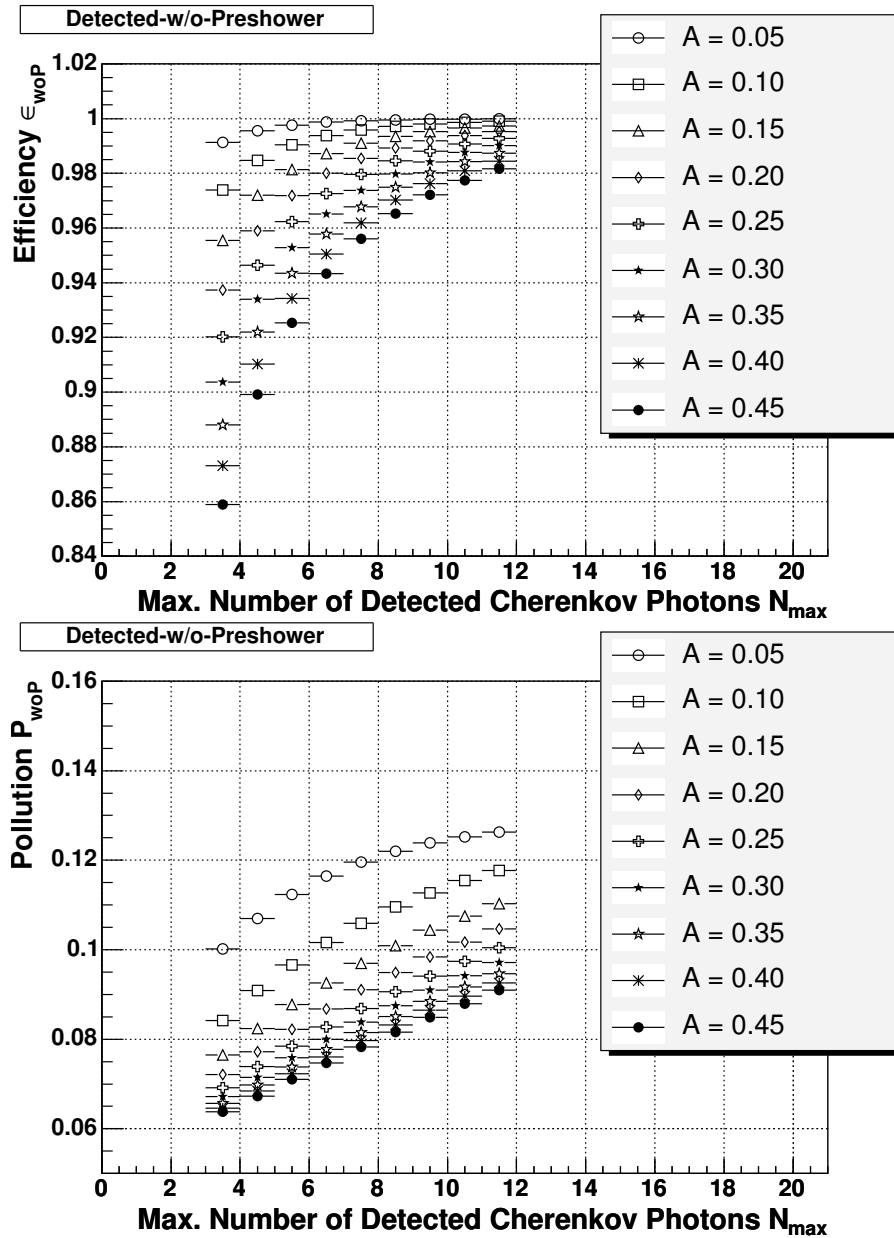


Figure 4.14: Identification efficiency and pollution obtained for the detected-w/o-preshower sample are shown in dependence of  $N_{\text{max}}$ . The different markers denote the various values of  $A_{\text{max}}$ .

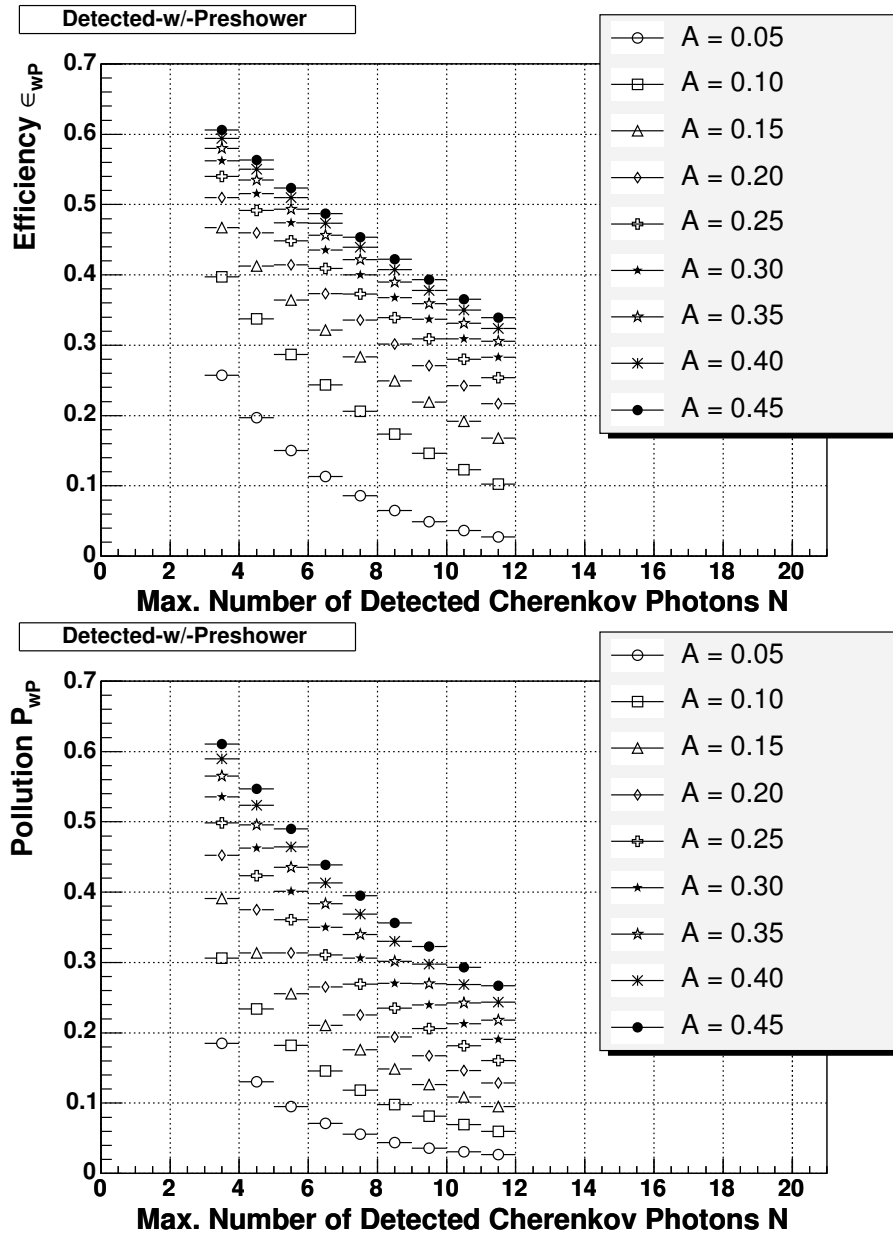


Figure 4.15: Identification efficiency and pollution obtained for the detected-w/-preshower are shown in dependence of  $N_{max}$ . The different markers denote the various values of  $A_{max}$ .

Using the values given above one obtains the efficiencies and pollutions listed in Table 4.3.

	<i>detected w/o preshower</i>	<i>detected w/ preshower</i>
$N_C$ with $A < 0.25$	$\leq 4$	$> 4$
$N_\gamma^{tot}$	89%	11%
$\epsilon$	94.6%	49.2%
$P$	7.4%	42.4%

**Table 4.3:** Results of the optimization process for a high identification efficiency and a low pollution.  $N_C$  is the number of detected Cherenkov photons associated to a cluster.  $N_\gamma^{tot}$  is the total fraction of photon clusters assigned to a sample.  $\epsilon$  and  $P$  are the efficiency and pollution respectively.

The number of clusters assigned to the *detected-w/-preshower* sample constitutes 11%. This sample contains almost 50% of all *generated-w/-preshower* photons. The total photon sample contains 13% of *generated-w/-preshower*. Thus, the fraction of photons which actually started to shower in front of the EMC is much enhanced in the *detected-w/-preshower* sample.

The *detected-w/o-preshower* sample contains 89% of all photon clusters. 95% of the *generated-w/o-preshower* photons are assigned to this sample. The fraction of *generated-w/-preshower* photons is 7% in this sample. Thus, the fraction of *generated-w/-preshower* photons is reduced by almost a factor of two compared with the overall sample.

The efficiency of the assignment of photons which did not shower in front of the calorimeter (*generated-w/o-preshower*) to the *detected-w/o-preshower* sample is high. 95% of the *generated-w/o-preshower* photons are identified. The number of remaining *generated-w/o-preshower* is reduced to 7%. Figure 4.16 shows the resulting fractions of clusters assigned to the *detected* samples.

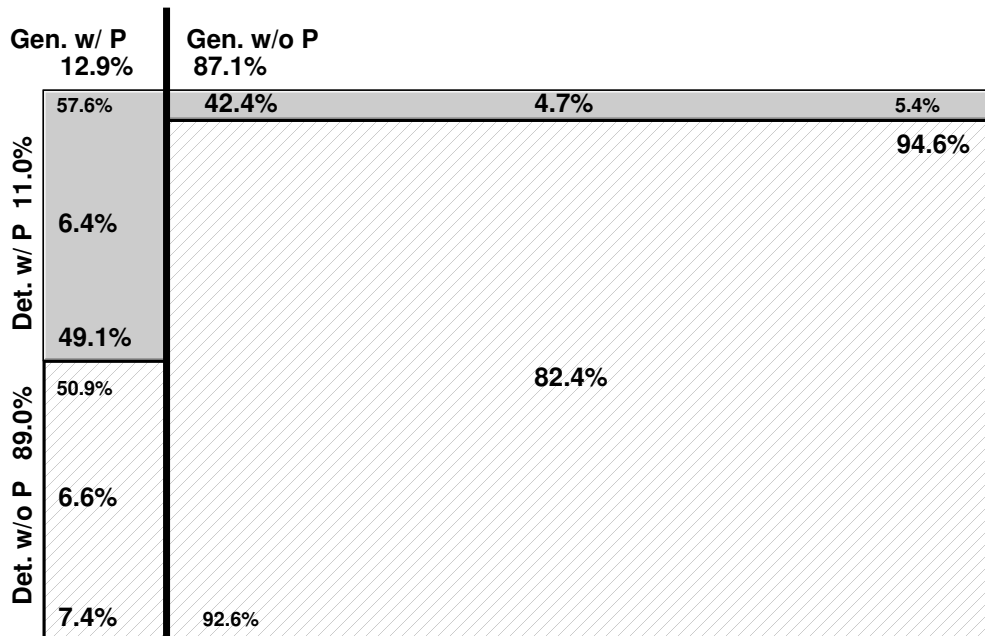


**Figure 4.16:** The total area of the box represents all clusters. The bold vertical line splits the total sample in two subsamples, on the left the clusters which were generated with preshowers (Gen. /w P 12.9%), on the right clusters which have been generated without preshowers (Gen. w/o P 87.1%). The horizontal lines also divide the total sample in two subsamples. The upper, shaded area represents clusters with detected preshowers (Det. w/ P 11.0%), the lower, hatched area clusters with no detected preshower (Det. w/o P 89.0%). The large numbers in the center of each of the four boxes describe the fraction of this sample with respect to the total sample, e.g., the number of clusters generated without preshower and detected without preshower is 82.4% of the total sample. The four value pairs at the borders of two subsamples describe the size of the two subsamples with respect to the sum of the two subsamples.

## 4.6 Summary

The objective of this chapter was the identification of photons which showered in front of the EMC, since these photons affect the photon energy resolution of the calorimeter. It was shown, that the fraction of this photons is 13 %. Almost all preshowers are started in the DIRC material. Thus, the approach to use the DIRC to identify this photons was studied. The Cherenkov light emitted in the DIRC-bars by  $e^+e^-$ -pairs emerging in the electromagnetic shower can be used to detect preshowers. The detected Cherenkov photons were associated to photon clusters. This procedure required several steps to suppress wrong assignments. Finally, photon clusters were discriminated in preshowers and photons which did not started to shower in front of the EMC using the number of associated Cherenkov photons. On optimization of the identification algorithm provided the result that preshowers have at least five associated detected Cherenkov photons. Based on Monte Carlo generator level information the quality of the identification was determined. 49 % of all preshowers were identified correctly. Thus, the fraction of true preshowers in the sample of photons which were detected as preshowers is enhanced by a factor of 3.8 compared with the total photon sample. After rejection of detected preshower photons, the remaining photon sample contains 7.4 % of true preshowers. Thus, the fraction of preshowers is reduced by almost a factor of two.

The next section presents two approaches to exploit this information. The first possibility is to study the impact of preshowers on the photon energy resolution. The second option is a correction of the photons energy depending on the number of associated Cherenkov photons to the considered cluster.

# Chapter 5

## Preshower corrections

### 5.1 Impact of preshowers on the photon energy resolution

This section studies the photon energy resolution for generic  $B^0\bar{B}^0$  Monte Carlo events in the *detected-w/o-preshower* and *detected-w/-preshower* samples. These samples can be used in further studies to analyze the description of preshowers in Monte Carlo simulations. They are also interesting for the  $\pi^0$  calibration described in Section 3.4.3 which suffers from the asymmetry in the  $m_{\gamma\gamma}$  distribution which is partially due to photons which showered in front of the EMC.

#### 5.1.1 Fitting procedure

In the following sections it is necessary to determine the width of various distributions with similar shapes, that means slightly asymmetric but mainly Gaussian peaks. In order to compare results it is necessary to find a well defined, stable and reproducible fitting procedure. The procedure described in this section is used for all peak fits. It allows to obtain the position of the peak and the width of the distributions which is a measure for the energy resolution. The fits are implemented to minimize  $\chi^2$  using MINUIT [10]. All errors on the estimators are the  $1\sigma$  standard deviations as computed by MINUIT.

At first the central part of the distribution is fitted with a Gaussian function in order to obtain an estimate for the peak position and the width. Then, the following function is fitted to the distribution:

$$f(\mu) = C \exp \left[ -\frac{1}{2} \left( \frac{\ln^2 \left( 1 + \frac{\sinh(\tau\sqrt{\ln 4}) (\mu - \mu_0)}{\ln 4 \sigma} \right)}{\tau^2} + \tau^2 \right) \right] \quad (5.1)$$

This function, further called *Novosibirsk Function*, has 4 parameters in total. The normalization constant  $C$ , the value of the peak position  $\mu$ ,  $\sigma$  which describes

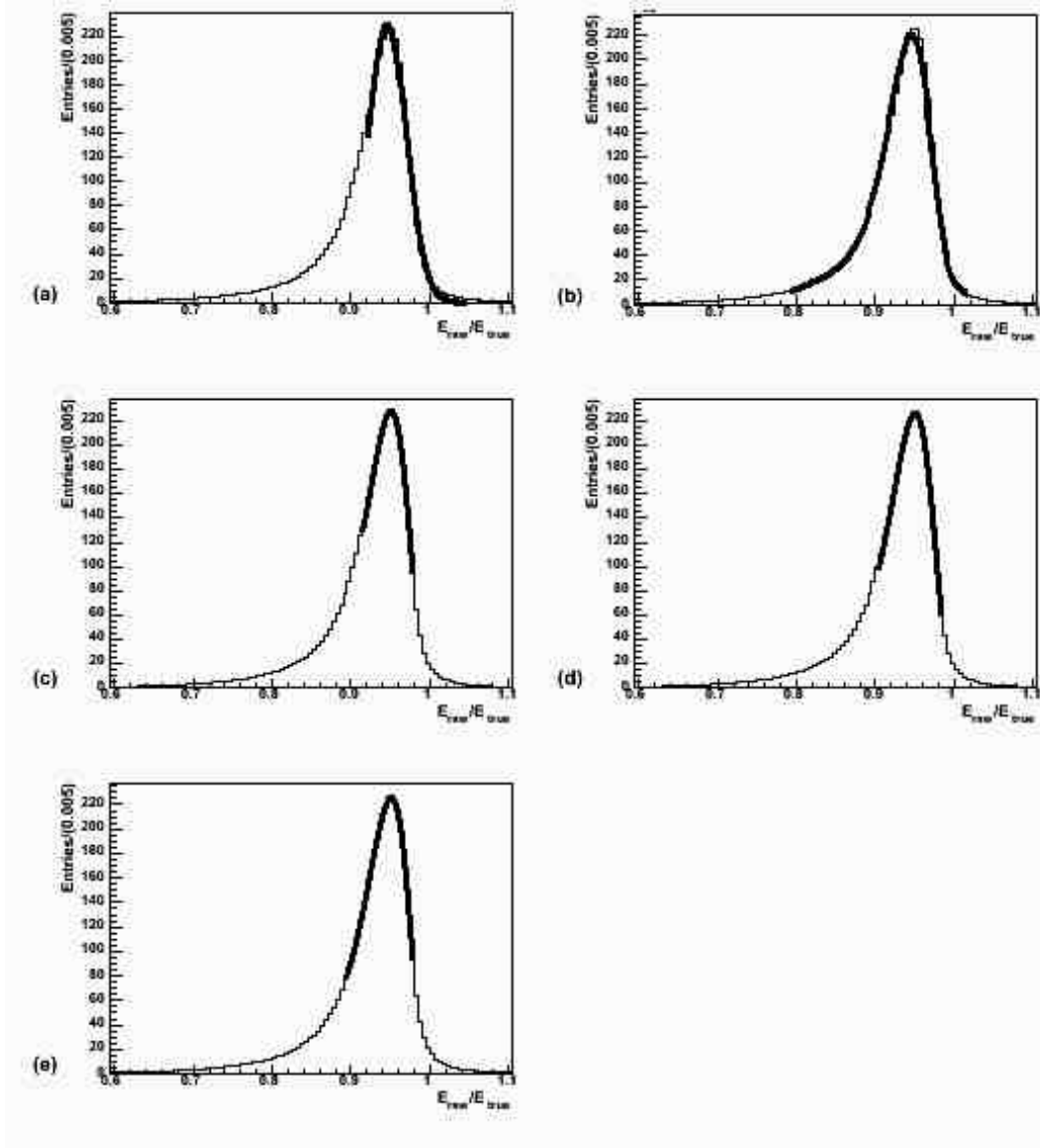


**Figure 5.1:** Photon energy distribution  $E_{raw}/E_{true}$  (generic  $B^0\bar{B}^0$  Monte Carlo). All steps of the chosen fitting procedure are shown. (a) Gaussian fit, (b-e) the Novosibirsk Function is fitted to the distribution in different ranges.

the width and the parameter  $\tau$ , which quantifies the size of the asymmetric *tail*. Essentially this function describes a Gaussian distribution with an additional asymmetric *tail*. The fit parameters determined in the Gaussian fit are used as start values for  $C$ ,  $\mu$  and  $\sigma$  of the *Novosibirsk Function*. This fit is applied in the range from 0.79 to 1.02 for all photon energy distributions. The next step is a further fit with the *Novosibirsk Function*. All start values for the parameters are obtained in the last fit. The fit is applied in the range  $[-1.2\sigma, +1.2\sigma]$ , where  $\sigma$  has the value obtained in the previous fit.

This step is repeated twice. However in a different range. The first iteration is applied in the interval  $[-1.7\sigma, +1.2\sigma]$ , the second in  $[-2.0\sigma, -1.0\sigma]$ . The range is varied to find a suited description of the peak. The considered distribution are slightly asymmetric, thus, the first iteration of the fit in an relatively tight symmetric range provides an estimate of the peak position. Then, the asymmetry of the fit range is increased to find a description of the decline of the peak to lower values. The position of the peak as well as sigma is obtained from the last fit. As an example, Figure 5.1 shows all fit steps for a photon energy distribution. The described procedure is applied to all photon energy distributions in order to guarantee a comparability of the results.

### 5.1.2 Photon energy resolution

In this section the energy distribution  $E_{raw}/E_{true}$  of the photons selected for this study (see Section 4.3) is compared with the energy distributions for the *detected* samples.

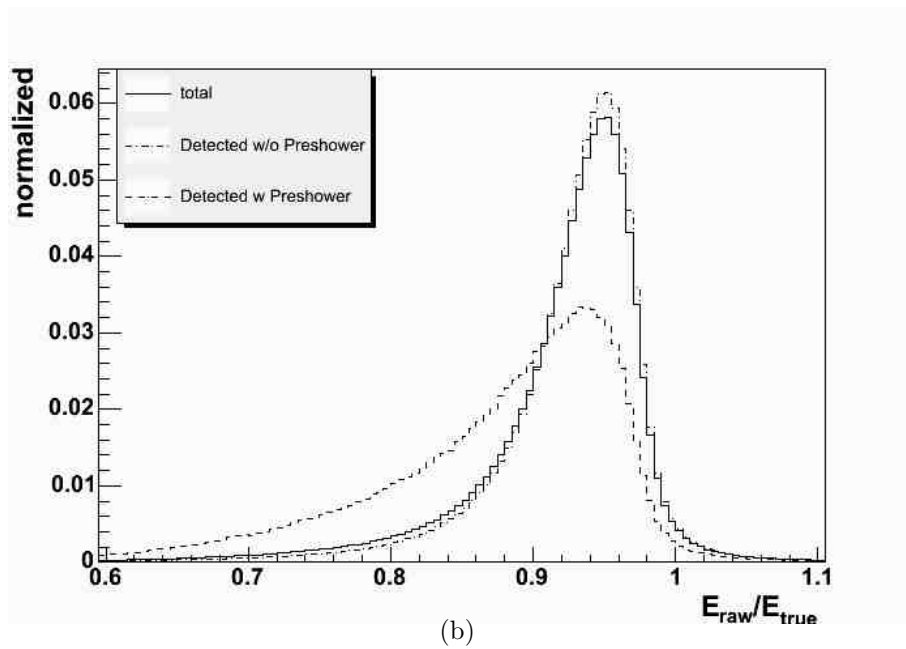
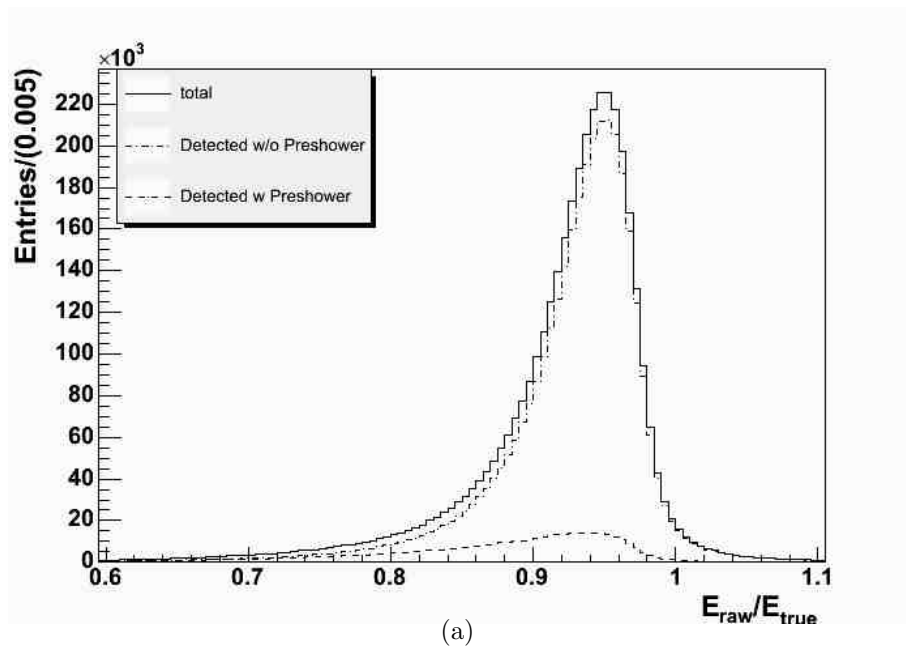
The Monte Carlo simulation provides the energy  $E_{true}$  which is the energy of the generated particle. The cluster energy  $E_{raw}$  is the energy obtained before the cluster corrections are applied. Thus, the peak in the photon energy distribution  $E_{raw}/E_{true}$  is not located at 1.0 but shifted to lower values.

Figure 5.2 shows the total energy distribution compared to the distributions of the two sub-samples. In (a) the ratio of the distributions can be seen. The histograms in (b) are scaled to unity to allow a comparison of shape. The large asymmetry of the *detected-w/-preshower* distribution is clearly visible.

The width and peak position of the distributions are determined in the fitting procedure described in Section 5.1.1. The fitted distributions are shown in Figure 5.3. Table 5.1 presents the fit results. The values of  $\chi^2/ndf$ , which describe the fit quality are not peaking around one, since small deviations of the fitting function from the distributions have a large effect in case of high statistics.

The fit results show that the peak position of the *detected-w/-preshower* distribution is shifted to lower values by 1.5% compared with the overall distribution. The width of the *detected-w/-preshower* distribution is larger by a factor of 1.8 compared to all clusters.

Photons which are believed to have started to shower in the DIRC are not contained in the *detected-w/o-preshower* sample. They do not contribute to the



**Figure 5.2:** Comparison of the three photon energy distributions  $E_{\text{raw}}/E_{\text{true}}$ . (a) shows the total, the detected-w/o-preshower and the detected-w/-preshower samples. For a better shape comparison, the three distributions are normalized to unit area in (b).

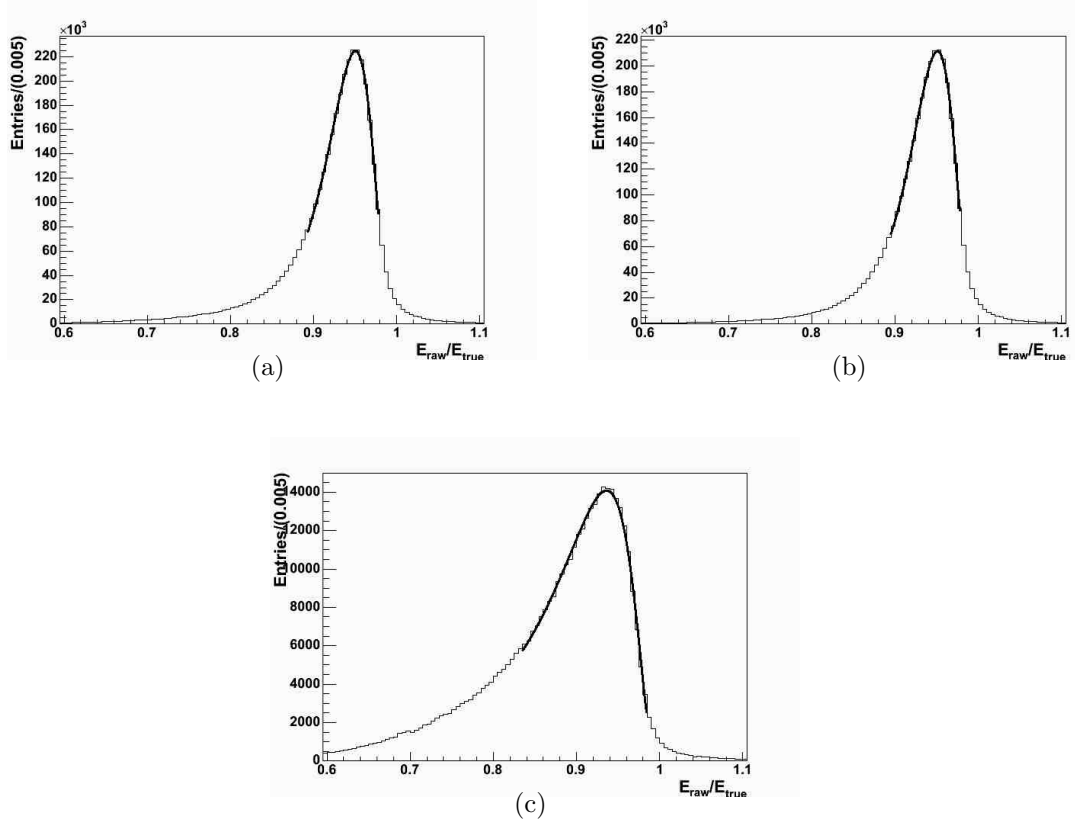


**Figure 5.3:** Last fitting step: The shown distributions are: (a) total , (b) detected-w/o-preshower , (c) detected-w/-preshower

	total	detected w/o preshower	detected w/ preshower
$\chi^2/\text{ndf}$	296/13	238/13	144/26
Peak Position	$0.9504 \pm 0.0001$	$0.9508 \pm 0.0001$	$0.9359 \pm 0.0002$
Sigma	$0.02853 \pm 0.00003$	$0.02769 \pm 0.00003$	$0.05105 \pm 0.00022$

**Table 5.1:** Results of the fits performed as described in Section 5.1.1.

energy distribution. Thus, a fraction of the photon energy distribution with a worse resolution is rejected. A consequence of this discrimination is a clearly visible reduction of the asymmetry in the *detected-w/o-preshower* distribution compared with the *total* distribution. By rejection of *detected-w/-preshower* clusters, the resolution of the energy distribution can be improved by 0.1% which is a relative improvement of 2.9%.

This results show that the applied method to identify preshowers leads to an improvement of the energy resolution. In the next section, the number of associated Cherenkov photons is not only used to discriminate between a *detected-w/o-preshower* and *detected-w/-preshower* sample, but to measure the energy loss  $\Delta E$  and correct the energy of photon clusters.

## 5.2 Energy correction

This section describes the development of an energy correction for photons with preshowers. The number of detected Cherenkov photons associated to a cluster provides a measure for the energy loss. The approach for the correction procedure is to measure the correlation between the number of detected Cherenkov photons and the energy loss and to obtain correction functions.

### 5.2.1 Binning

Since the idea is to transform the number of associated DIRC-hits into a value  $\Delta E_{lost}$  which can be used to correct the reconstructed photon energy, it is necessary to identify other variables which are correlated to the number of detected Cherenkov photons. The number  $N_C$  is also correlated with the polar angle  $\theta$  of the cluster centroid and to the total energy of the cluster.

A particle which traverses a DIRC-bar at normal incident passes less material than a particle which enters the DIRC with a larger  $|\cos\theta|$  value. The number of emitted Cherenkov photons increases with the amount of passed radiation lengths. The energy loss  $\Delta E$  increases. This effect keeps the proportionality of the number of Cherenkov photons to  $\Delta E$ . Figure 5.4 shows the number of DIRC-hits in dependence of the  $\Theta$  coordinate for clusters with the same amount of energy lost in the DIRC (30 MeV - 40 MeV) in order to exclude the influence of the effect described above. A  $\theta$  dependence is clearly visible. The number of DIRC-hits has a minimum at 90 degrees and increases with larger  $|\cos\theta|$  values. This is due to the effect that the efficiency of the DIRC to detect Cherenkov photons changes with the entrance coordinate of the particle. The fraction of detected DIRC-photons varies with  $|\cos\theta|$ . With higher  $|\cos\theta|$  values more Cherenkov photons are trapped by the internal reflection.

In order to account for the  $\Theta$  dependence due to the varying detection efficiency, six equidistant bins (Table 5.2) are defined in the region of the calorimeter which is covered by the DIRC.

Bin	$\Theta$ Range [rad]
0	0.473 - 0.804
1	0.804 - 1.135
2	1.135 - 1.466
3	1.466 - 1.797
4	1.797 - 2.128
5	2.128 - 2.456

**Table 5.2:**  $\Theta$  bins for the energy correction process.

Since there is residual background in the association of detected Cherenkov

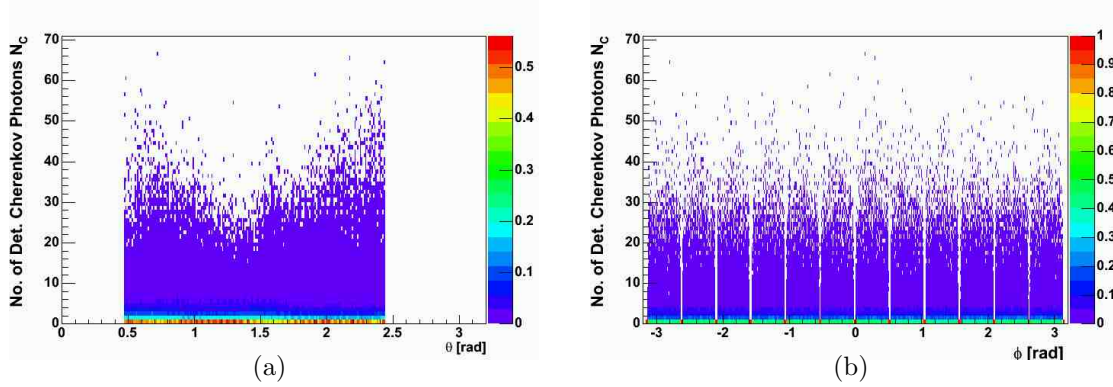


**Figure 5.4:** (a) Number of detected Cherenkov photons associated to a cluster versus the the polar angle  $\theta$ . (b) The number of detected Cherenkov photons is plotted versus the azimuth angle  $\phi$ : The stripes in the distribution are due to the gaps between the 12 DIRC-bars.

photons, it might be possible, that there is also a global  $\phi$  dependence. Due to synchrotron radiation of the beam in the complicated beam path in the vicinity of the interaction region, the DIRC has a higher occupancy at the inward direction. Figure 5.4 shows that there is no correlation of the number of detected Cherenkov photons to  $\phi$ . The number  $N_C$  is flat as a function of  $\phi$ .

Finally, the correlation to the total energy  $E_{raw}$  of the cluster is taken into account. To first order, the amount of energy deposited in a relatively thin layer of material as the DIRC should be independent of the momentum of the particle. Still, when measuring the correlation between the number of detected Cherenkov photons and the energy loss in bins of  $E_{raw}$  a slight dependence has been found. Thus, it was chosen to compute the correction functions in three bins of energy. The bins are given in Table 5.3. The resulting number of bins which are chosen

Bin	Energy Range [GeV]
0	0.1 - 0.4
1	0.4 - 0.7
2	>0.7

**Table 5.3:** The energy correction is applied in three energy bins.

for the energy correction process is 6  $\Theta$  bins times 3 energy bins. Thus, the total number is 18.

### 5.2.2 Determination of correction coefficients

The photon clusters considered for the energy correction are the clusters assigned to the *detected-w/-preshower* sample (see Section 4.5.1). That means clusters which have at least five associated Cherenkov photons.

In each of the 18 bins discussed in the last section the following algorithm is applied in order to determine correction constants.

For each cluster assigned to the *detected-w/-preshower* sample the energy loss  $\Delta E$  as defined in Equation 5.2 is plotted versus the number of Cherenkov photons associated to the cluster.

$$\Delta E = E_{raw} - E_{true} \quad (5.2)$$

Figure 5.5 shows a example of such a distribution for one of the 18 bins. The

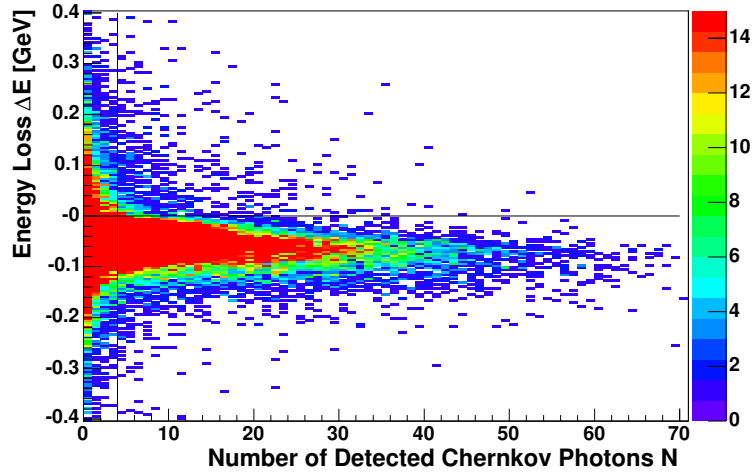


**Figure 5.5:** Cluster energy loss  $\Delta E$  versus the number of associated Cherenkov photons  $N_C$ . This histogram is an example for 18 distributions in total: The shown  $\theta$  bin is  $(0.473-0.804)$  rad, the photon cluster energy range is  $(400-700)$  MeV. The correlation of the two quantities is clearly visible. A large number of Cherenkov photons corresponds to a higher energy loss. The vertical line marks  $N_{max} = 4$ . Clusters which lie to the right from this line are assigned to the *detected-w/-preshower* sample. They are considered for the correction step.

correlation between the number of detected Cherenkov photons and the energy loss is clearly visible. This histogram is splitted in vertical slices with a width of five Cherenkov photons. The low edge of the first slice is determined by  $N_{max} = 4$  which is the maximum number of Cherenkov photons associated to a cluster in the *detected-w/o-preshower* sample. For each slice the  $\Delta E$  distribution is fitted to determine the position of the peak. The number of entries in such a histogram is

required to be larger than 60 to assert a stable fit. Slices with a smaller number of contributing clusters are rejected from the succeeding steps. The used fit function is the *Novosibirsk Function* which is described in Section 5.1.1. As an example, four fitted distributions (out of the total number of 135) are shown in Figure 5.6.

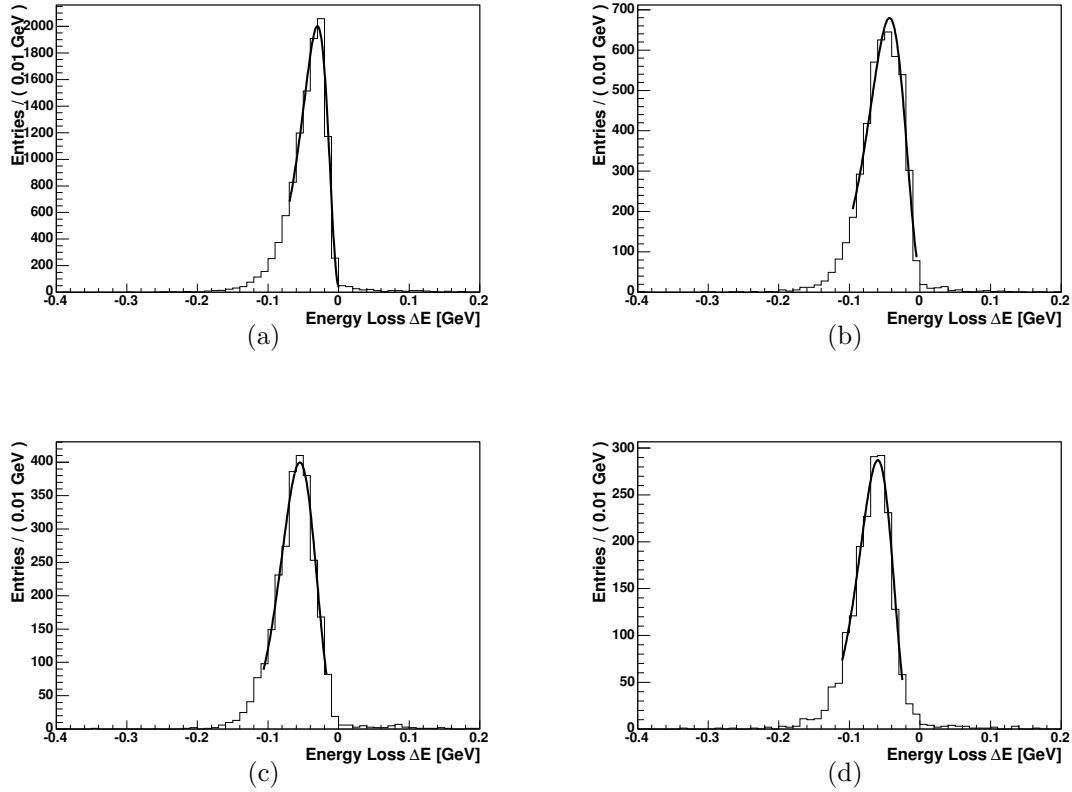


**Figure 5.6:** Example of the energy loss distribution obtained for different intervals of the number of Cherenkov photons associated to clusters: **(a)** [5,9], **(b)** [10,14], **(c)** [15-19], **(d)** [20-24]. The chosen photon energy range is (400-700) MeV. The polar angle  $\theta$  interval is (0.473-0.804) rad.

The peak position obtained by the fit is then plotted against the number of Cherenkov photons (square markers in Figure 5.7). Then a linear function is fitted to the resulting distribution. The slope  $S$  of this function is used as the correction constant. The determined values are given in Table 5.4. The constant term obtained in the fit is not used any further. This constant value is not zero due to the missing cluster calibration. The cluster energy corrections described in Section 3.4.3 would cause a shift of the total distribution by a factor which is similar to the constant term of the linear fitting function.

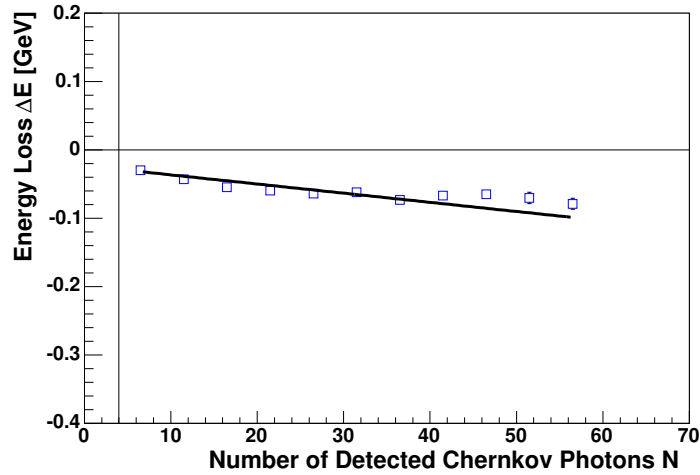


**Figure 5.7:** *The mean energy loss obtained from a fit with a Novosibirsk Function versus the number of detected Cherenkov photons. The distribution is fitted with a linear function. The determined slope provides a correction constant in these bins. As an example, the same  $\theta$  and energy intervals are chosen as for Figure 5.5.*

$S [10^{-3}]$	0	1	2
0	$1.98 \pm 0.01$	$1.34 \pm 0.04$	$1.30 \pm 0.07$
1	$1.98 \pm 0.02$	$1.34 \pm 0.05$	$1.05 \pm 0.11$
2	$2.18 \pm 0.05$	$0.80 \pm 0.11$	$0.65 \pm 0.17$
3	$1.90 \pm 0.03$	$0.81 \pm 0.08$	$0.87 \pm 0.19$
4	$1.46 \pm 0.04$	$0.83 \pm 0.06$	$0.71 \pm 0.19$
5	$1.38 \pm 0.02$	$0.92 \pm 0.06$	$0.79 \pm 0.27$

**Table 5.4:** *The energy correction constants are the slopes of the linear fits shown in Figure 5.7*

Figure 5.8 shows all energy loss distribution depending on the number of associated Cherenkov photons. The determined peak positions in slices as well as the linear fit are shown.

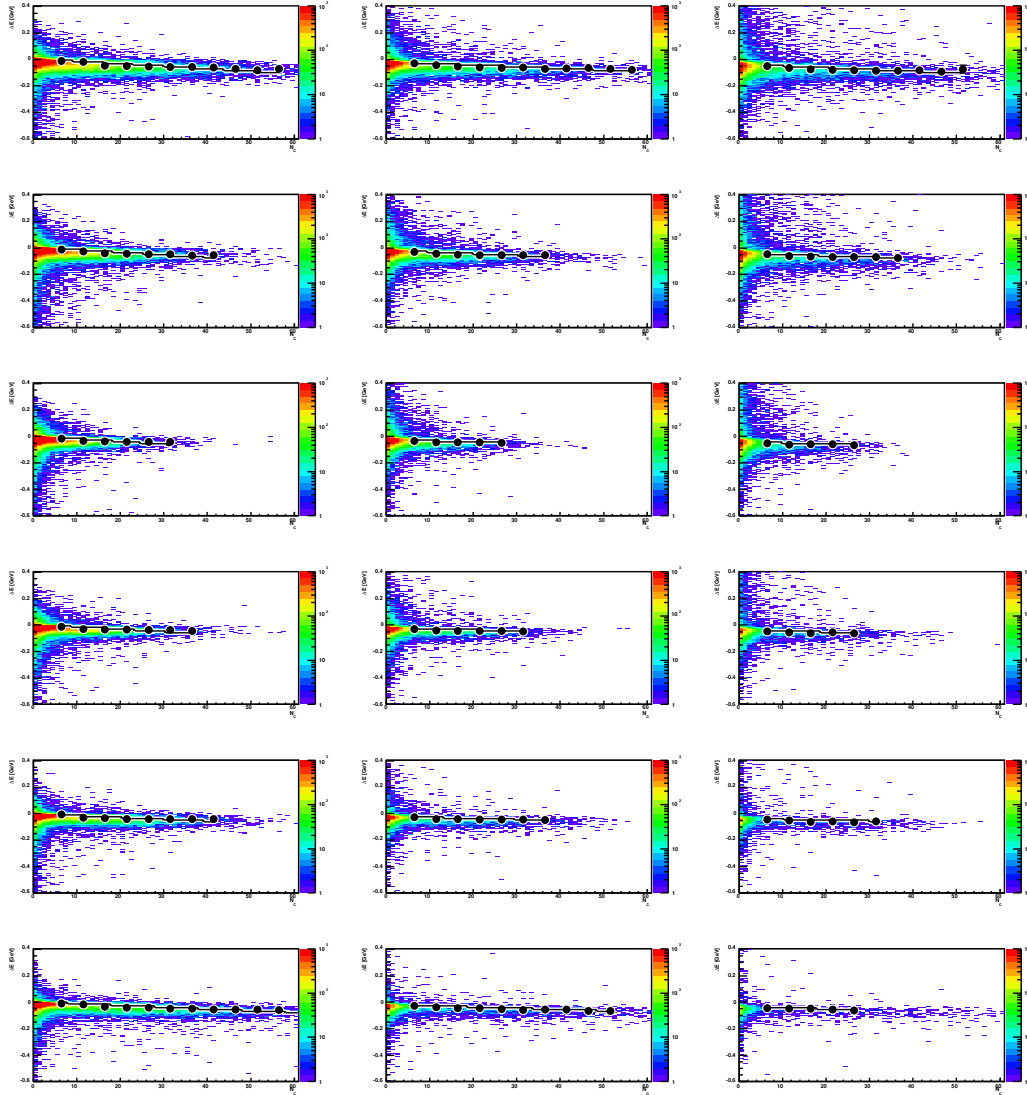


**Figure 5.8:** Energy loss  $\Delta E$  versus the number of detected Cherenkov photons. The distributions in all bins for the energy correction are shown. The columns from left to right correspond to the energy bins (Table 5.3). The rows from top to bottom correspond to the  $\theta$  bins (Table 5.2).

### 5.2.3 Verification

The following formula is used to correct the energy of a cluster which is contained in one of the 18 bins:

$$E_{COR} = E_{raw} + S_i \cdot N_C \quad (5.3)$$

where  $S_i$  is one of the correction constants (Table 5.4) for a certain bin and  $N_C$  is the number of detected Cherenkov photons associated to a cluster.

The energy correction code has been verified by applying the corrections and repeating the whole procedure. Figure 5.9 shows an example of an energy loss distribution in dependence of the number of Cherenkov photons associated to a cluster with an corrected energy. The resulting slope of the peak position is zero (Figure 5.10). That means, no additional correlation has been found.

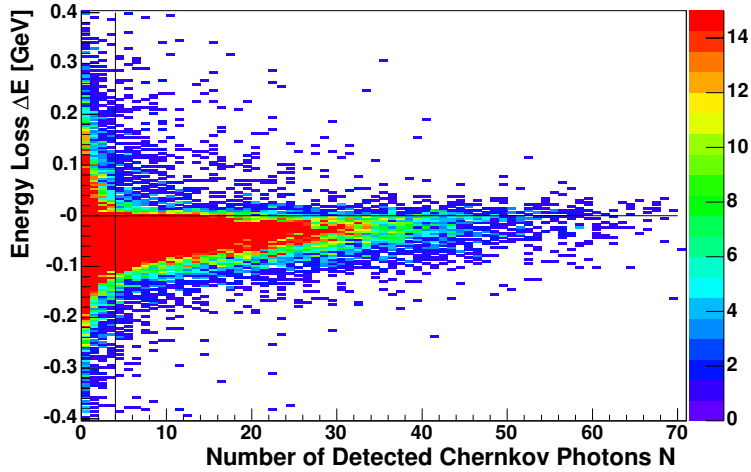


**Figure 5.9:** Energy loss  $\Delta E$  versus number of detected Cherenkov photons after correction. The chosen photon energy range is (400-700) MeV. The polar angle  $\theta$  interval is (0.473-0.804) rad.

### 5.2.4 Impact on the photon energy resolution

This section describes the effect of the energy correction on the photon energy resolution  $E_{raw}/E_{true}$ .

The fitted corrected *detected-w/-preshower* and the corrected total distribution are shown in Figure 5.11. The obtained values for the peak position and the width are shown in Table 5.5.

Figure 5.12 compares the *detected-w/-preshower* with the corrected *detected-w/-preshower* distribution. The asymmetric shape is lost after correction. The corrected *detected-w/-preshower* distribution is clearly shifted to higher values by a factor of 1.03. A comparison with the *detected-w/o-preshower* distribution

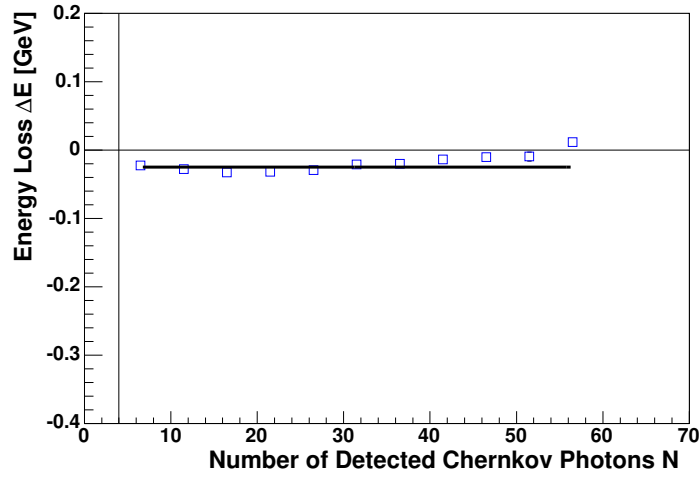


**Figure 5.10:** *Determined peak value of the energy loss versus the number of detected Cherenkov photons after correction. The same bin is shown as in Figure 5.9.*

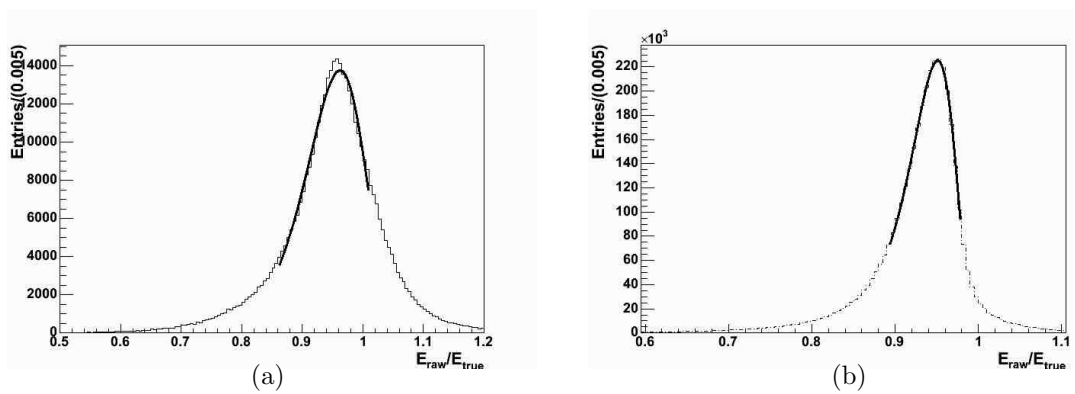


**Figure 5.11:** *(a) shows the fitted detected-w/-preshower distribution after correction. In (b) the fitted total distribution  $E_{raw}/E_{true}$  is shown, after the correction has been applied.*

	<b>total</b>	<b>total corrected</b>
$\chi^2/\text{ndf}$	296/13	304/13
Peak Position	$0.9504 \pm 0.0001$	$0.9510 \pm 0.0001$
sigma	$0.02853 \pm 0.00003$	$0.02824 \pm 0.00003$
	<b>detected-w/-preshower</b>	<b>detected w/ preshower corrected</b>
$\chi^2/\text{ndf}$	144/26	492/26
Peak Position	$0.9360 \pm 0.0002$	$0.9622 \pm 0.0002$
sigma	$0.05105 \pm 0.00022$	$0.04943 \pm 0.00023$

**Table 5.5:** *Fitting results before and after the application of the correction.*

shows that the peak is shifted to the peak position of the *detected-w/o-preshower* distribution.

The resolution of the overall photon energy distribution is improved by 1.0% (relative) after correction.

The effect of the energy correction on the total photon sample is smaller than the effect of the rejection of preshowers described in Section 5.1.2. However, the parameters A and N were not optimized with regard to the energy correction. The goal was a balanced relation between the efficiencies of the two *detected* samples. A specific optimization for a high identification rate of photons which showered in front of the electromagnetic calorimeter and a low pollution of this sample could improve the enhancements in the energy resolution.

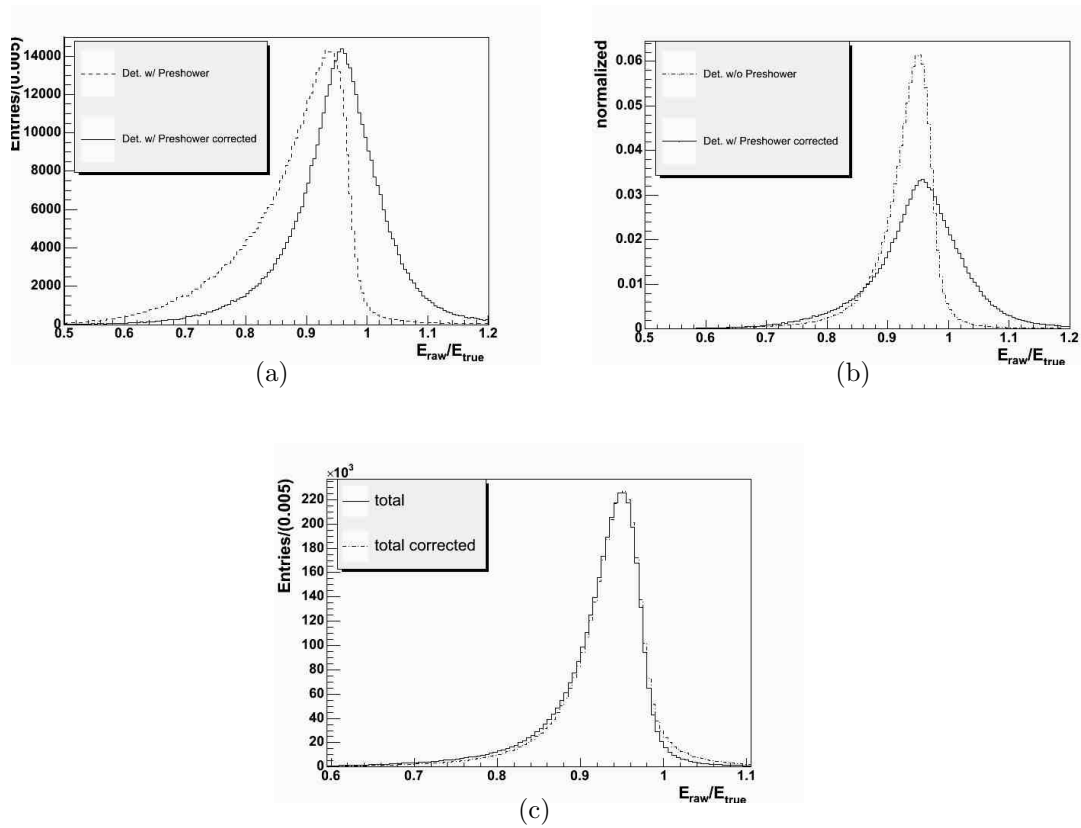


**Figure 5.12:** Comparison between the following distributions: (a) uncorrected and corrected detected-w/-preshower, (b) uncorrected and corrected detected-w/o-preshower, (c) total before and after correction.

### 5.3 Comparison of data with simulation

The development of the Cherenkov-photons-to-clusters association, the discrimination of two samples of photons, as well as the determination of energy correction constants was based on Monte Carlo simulations. The generator level information available in the simulation was necessary to obtain the efficiencies and pollutions of the assignment of the clusters to the *detected* samples. Also, the energy loss of photons which started to shower in the DIRC was defined as the difference between the energy deposited in the calorimeter and the generator level energy. The impact of the preshower corrections on the photon energy resolution was also studied by comparing the energy distributions with the generator level information. The whole procedure needs to be verified on data. Since it is not very easy to measure the energy resolution of single photons in data the  $\pi^0$  mass distribution is used to compare data and Monte Carlo.  $\pi^0$ -mesons are abundant and easy to reconstruct. The width of the mass distribution is relatively easy to measure and no generator level information is needed.

#### 5.3.1 $\pi^0$ mass distribution

The following equation is used for the  $\pi^0$  mass reconstruction.

$$m_{\pi^0}^2 = 2E_{\gamma,1}E_{\gamma,2}(1 - \cos \alpha) \quad (5.4)$$

The measured deposited energy of the photons and the angle between the photon directions allow the reconstruction of the mass which is called  $m_{\gamma\gamma}$  in the following.

The clusters are selected as described in section 4.3. The selection criterion that no second cluster should be within 15 degrees with respect to the considered cluster affects the  $(1 - \cos \alpha)$  term in Equation 5.4. Normally, the minimal value for this term is defined by the ability of the electromagnetic calorimeter to separate photons. However, the above requirement increases this minimal value to 0.03. Thus, small values for the reconstructed mass  $m_{\gamma\gamma}$  are slightly suppressed.

The used  $m_{\gamma\gamma}$  reconstruction algorithm combines each cluster with all other clusters in the event. This procedure leads to a combinatorial background. A value for  $m_{\gamma\gamma}$  is also calculated even if one or both of the combined clusters does not originate from a  $\pi^0$ -meson. An algorithm developed by Dr. Jörg Marks [11] allows to subtract the combinatorial background from the  $m_{\gamma\gamma}$  distribution. Each cluster in a certain event is combined with each cluster from the next event. The resulting distribution describes the background, since the energy distribution and multiplicity of clusters is the same but no  $\pi^0$  can be reconstructed. In the next step the integral of the original distribution in a range outside the signal region is determined. The value of the integral is used to scale the background which is then subtracted from the original  $m_{\gamma\gamma}$  distribution. This distribution is shown in Figure 5.13 together with the combinatorial background. The  $\pi^0$  mass does peak

at 135 MeV. This is expected as  $E_{raw}$  (see Section 4.1) is used for the cluster energy.

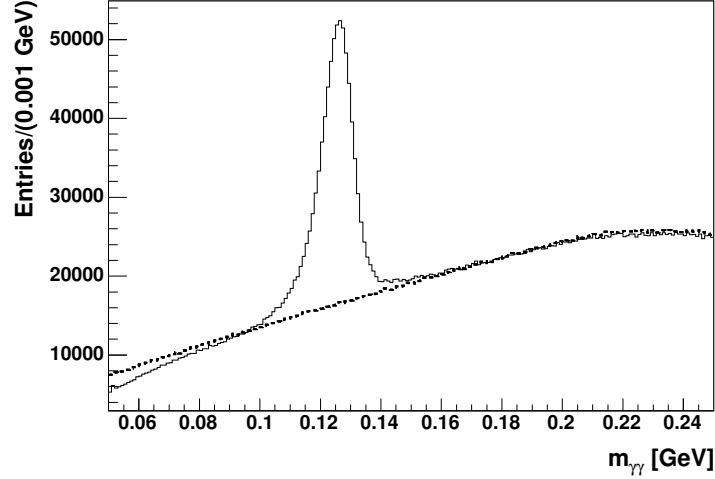


**Figure 5.13:** Original  $m_{\gamma\gamma}$  distributions (solid) and combinatorial background from mixed events (dashed).

This background subtraction is performed in order to apply a reasonable fitting procedure to the distributions. In the following the same iterative fitting procedure as described in Section 5.1.1 is applied in order to obtain the peak position and the width of the  $m_{\gamma\gamma}$  distribution.

### 5.3.2 $\pi^0$ -mesons with preshowers

$\pi^0$ -mesons are reconstructed from photons which were assigned to the *detected-w/o-preshower* or the *detected-w/-preshower* sample (see Section 4.5.1).

A  $\pi^0$  is called *detected-w/o-preshower* if both photons were assigned to the *detected-w/o-preshower* sample. For a *detected-w/-preshower*  $\pi^0$  at least one of the two photons is required to be *detected-w/-preshower*.

*detected-w/o-preshower*  $\pi^0$  : both photons are *detected-w/o-preshower*

*detected-w/-preshower*  $\pi^0$  : at least one photon is *detected-w/-preshower*

The expected maximum number of  $\pi^0$ -mesons assigned to the *detected-w/-preshower* sample can be estimated from the fraction of photons which are *detected-w/-preshower*. This fraction is 11% (see Section 4.5.3). Thus, the expected value for the number of *detected-w/-preshower*  $\pi^0$ -mesons is 21%.

Table 5.6 gives the determined fraction of *detected-w/-preshower*  $\pi^0$ -mesons for Monte Carlo as well as for data. The numbers show a good agreement. This

	<b>fraction of <i>detected-w/-preshower</i> <math>\pi^0</math>-mesons [%]</b>
Monte Carlo	20.9
Data	19.5

**Table 5.6:** Fraction of *detected-w/-preshower*  $\pi^0$ -mesons in the total  $\pi^0$  sample

result is a further indication that the procedure of the association of detected Cherenkov photons to clusters can be transferred to real data.

### 5.3.3 Impact of the preshower identification on the $\pi^0$ mass distribution in data and simulation

This section discusses the impact of the preshower identification applied on the  $\pi^0$  mass distribution in Monte Carlo and data. Figure 5.14 compares the distributions for the total, the *detected-w/o-preshower* and the *detected-w/-preshower*  $\pi^0$  samples. The combinatorial background is subtracted as described in Section 5.3.1. The histograms are scaled to unity.

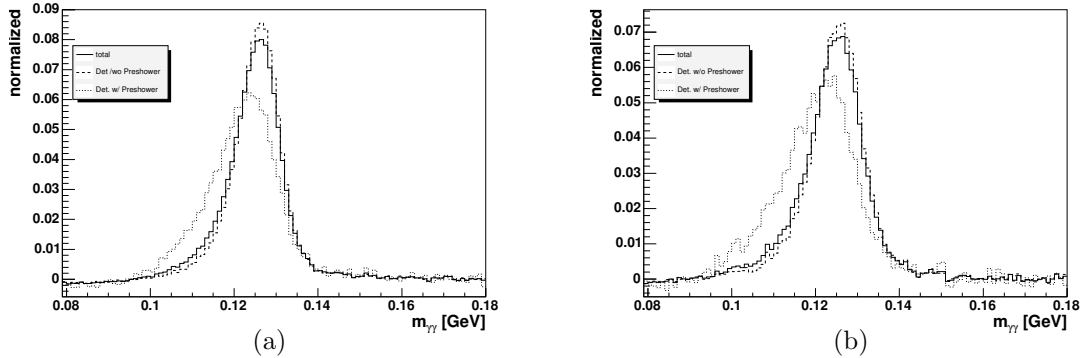


**Figure 5.14:** Comparison between  $m_{\gamma\gamma}$  distributions for Monte Carlo (a) and data (b)

The resolution of the total  $m_{\gamma\gamma}$  distribution suffers from the combination of *detected-w/o-preshower* photons with *detected-w/-preshower* photons as well as from the combination of two *detected-w/-preshower* photons. The latter double the effect of the energy loss in front of the calorimeter. In the *detected-w/o-preshower*  $\pi^0$  sample both combination types are rejected. Thus, it is expected that the improvements of the resolution for the *detected-w/o-preshower*  $\pi^0$  sample are larger than for the *detected-w/o-preshower* photon distribution discussed

in section 5.2.4. One of the two photons from which a *detected-w/-preshower*  $\pi^0$  is reconstructed from is allowed to be *detected-w/o-preshower*. Thus, the distribution of the *detected-w/-preshower*  $\pi^0$ -mesons is expected to show a smaller asymmetry effect as the *detected-w/-preshower* photon distribution.

The results of the fitting procedure (see Table 5.7) which is applied according to the method described in Section 5.1.1 verify these expectations for Monte Carlo as well as for real data. The fitted distributions are shown in Figure 5.15 for Monte Carlo data and in Figure 5.16 for real data.

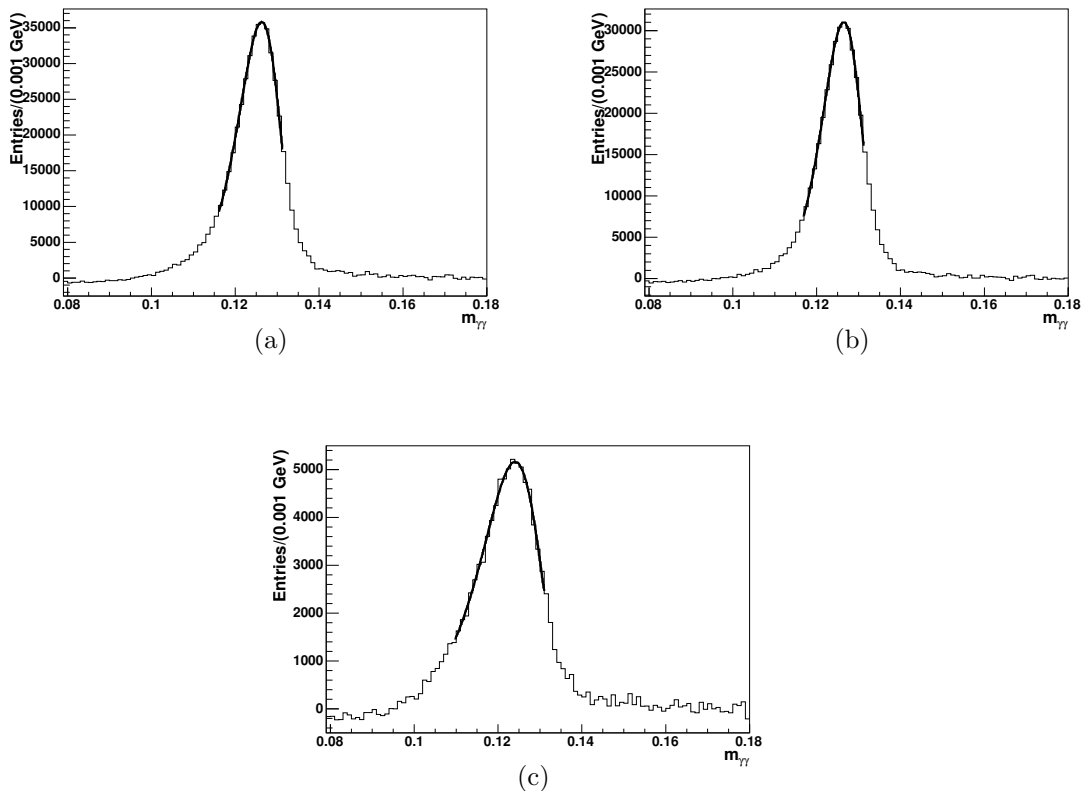


**Figure 5.15:** Generic  $B^0\bar{B}^0$  Monte Carlo:  $m_{\gamma\gamma}$  distributions fitted as described in Section 5.1.1: (a) total, (b) *detected-w/o-preshower* and (c) *detected-w/-preshower*. The fits are of good quality (see Table 5.7).

Figure 5.17 compares the three  $m_{\gamma\gamma}$  distributions for data and Monte Carlo events. The slight differences in the  $m_{\gamma\gamma}$  distributions for data and Monte Carlo simulations are expected [12]. Other studies show that the detector response differs in data and Monte Carlo. However, the broadening of the distribution in the  $\pi^0$  sample with preshowers in data is nicely reproduced in the Monte Carlo

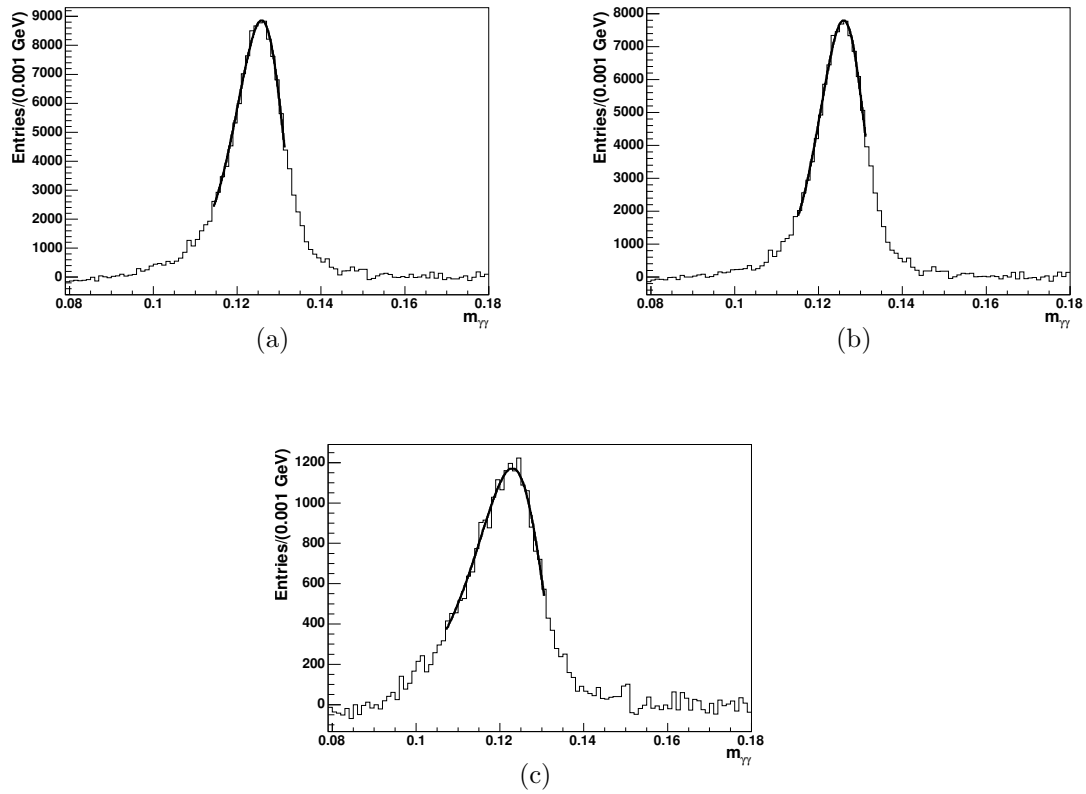


**Figure 5.16:** Real data:  $m_{\gamma\gamma}$  distributions: (a) total, (b) detected-w/o-preshower and (c) detected-w/-preshower.

	total	detected w/o preshower	detected w/ preshower
<b>Monte Carlo</b>			
$\chi^2/\text{ndf}$	25/11	11/10	58/17
peak Position	$0.1263 \pm 0.00002$	$0.1265 \pm 0.00002$	$0.1241 \pm 0.0001$
sigma	$0.0050 \pm 0.00002$	$0.004728 \pm 0.000024$	$0.007021 \pm 0.000057$
<b>Data</b>			
$\chi^2/\text{ndf}$	65/13	32/12	48/20
peak Position	$0.1259 \pm 0.00005$	$0.1260 \pm 0.00005$	$0.1230 \pm 0.00016$
sigma	$0.005633 \pm 0.000047$	$0.005369 \pm 0.000054$	$0.007918 \pm 0.000112$

**Table 5.7:** Fitting results for the  $m_{\gamma\gamma}$  distributions in the Monte Carlo simulation and in data.

simulation.

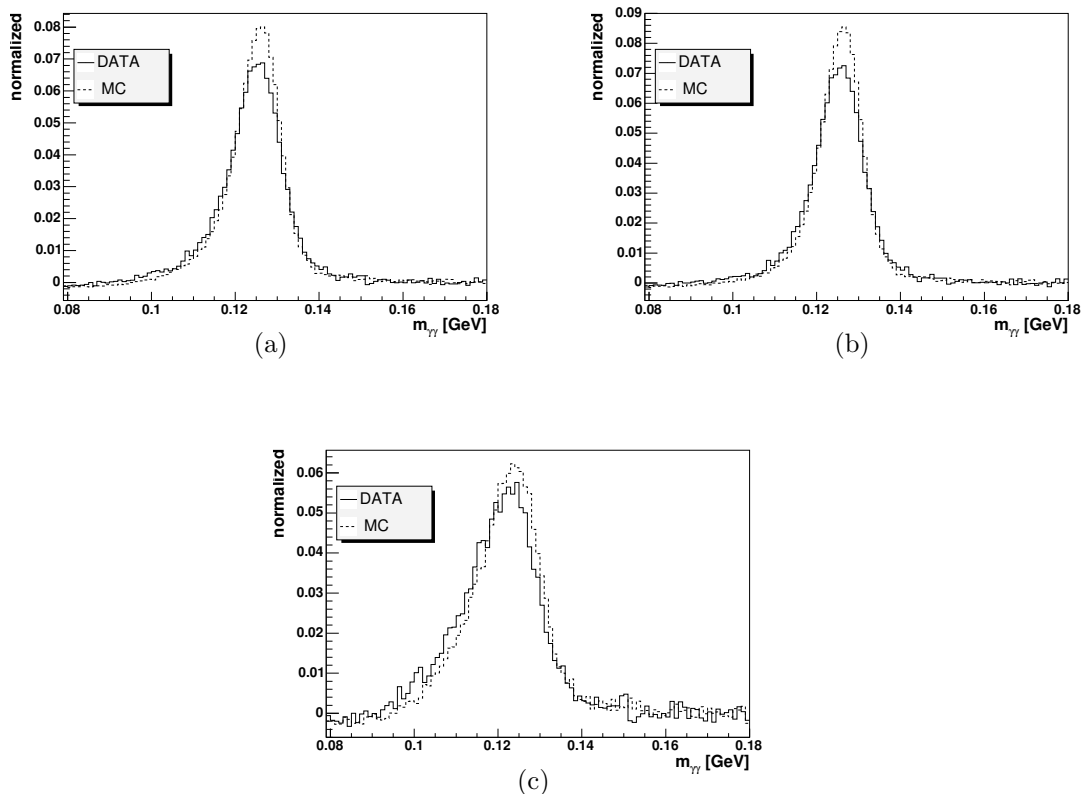


**Figure 5.17:** Comparison between  $m_{\gamma\gamma}$  distributions in data (solid) and Monte Carlo (dashed). (a) total, (b) detected-w/o-preshower, (c) detected-w/-preshower.

### Monte Carlo

A comparison of the *detected-w/-preshower*  $\pi^0$  distribution with the total  $\pi^0$  distribution shows that the peak position of the dirty  $\pi^0$ s is shifted to lower values by 1.7%. Sigma is larger by a factor of 1.4%. The *detected-w/o-preshower* sample shows a relative resolution improvement of 5.4% compared with the total distribution.

### Data

For data similar results are obtained as for the Monte Carlo sample. The peak position of the dirty distribution is shifted by 2.3% to lower values. The higher

asymmetry is clearly visible. The achieved relative improvement of the *detected-w/o-preshower* distribution is 4.7%.

### Conclusion

The discrimination of photons which showered in front of the EMC from photons which reached the calorimeter is feasible in Monte Carlo as well as in data. The resolution of the  $m_{\gamma\gamma}$  distribution is improved for the *detected-w/o-preshower*  $\pi^0$  sample. The asymmetry is reduced. The *detected-w/-preshower* sample is enhanced with photons which showered in front of the EMC. Thus, both samples are suitable for further studies like the investigation of systematic uncertainties in the description of the asymmetry in Monte Carlo. These samples are also interesting for the  $\pi^0$  *calibration* which suffers from the asymmetry in the  $\pi^0$  mass distribution.

### 5.3.4 Impact of the energy correction on the $\pi^0$ mass distribution in data and simulation

The Monte Carlo study described in Section 5.2 showed that an energy correction depending on the number of clusters is possible and leads to an improvement of the energy resolution.

The energy correction is also tested for the reconstructed  $m_{\gamma\gamma}$  distribution for data and Monte Carlo simulations. Figure 5.18 and Figure 5.19 show the fitted distribution after correction for the *detected-w/-preshower*  $\pi^0$ s and the total sample for the Monte Carlo simulation as well as for data. The fitting results are listed in Table 5.8.

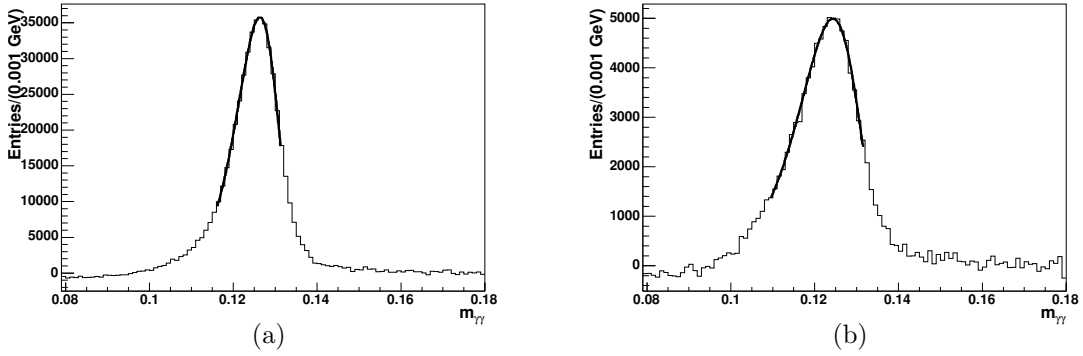


**Figure 5.18:** *Generic  $B^0\bar{B}^0$  Monte Carlo: (a) corrected detected-w/-preshower distribution and (b) corrected total distribution. A fit is applied according to the method described in Section 5.1.1*

	<i>detected w/ preshower corrected</i>	<i>total corrected</i>
<b>Monte Carlo</b>		
$\chi^2/\text{ndf}$	53/18	26/11
Peak Position	$0.1244 \pm 0.0001$	$0.1264 \pm 0.00002$
Sigma	$0.007257 \pm 0.000053$	$0.004979 \pm 0.000022$
<b>Data</b>		
$\chi^2/\text{ndf}$	70/20	35/12
Peak Position	$0.1235 \pm 0.0002$	$0.1258 \pm 0.00005$
Sigma	$0.008087 \pm 0.0000129$	$0.005628 \pm 0.00005$

**Table 5.8:** *Fitting results for the  $m_{\gamma\gamma}$  distributions.*

The energy correction of the *detected-w/-preshower* photons from which the  $\pi^0$  mass is reconstructed causes a degradation of the sigma of the *detected-w/-*

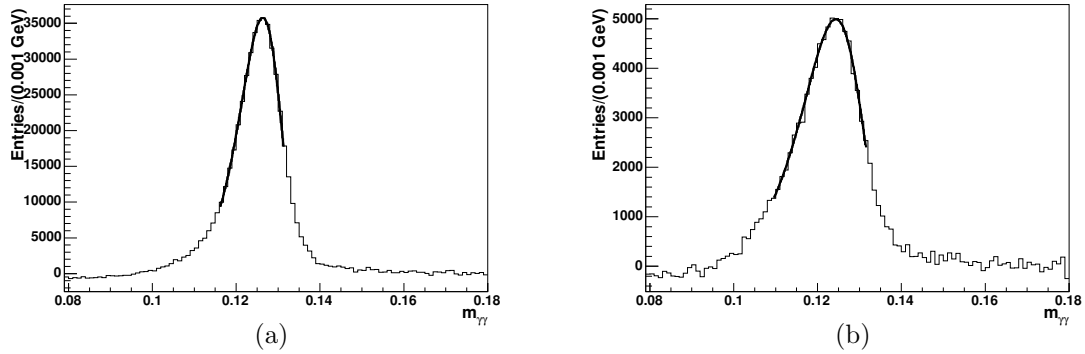


**Figure 5.19:** Data: **(a)** corrected detected w/-preshower distribution and **(b)** corrected total distribution. A fit is applied according to the method described in Section 5.1.1.

preshower  $\pi^0$  distribution after correction by a factor of 1.03 in Monte Carlo and 1.02 in data. The peak is not significantly shifted to higher values. The comparison (Figure 5.20 and 5.21) of the overall distribution before and after correction shows no effect on the peak position and resolution for Monte Carlo as well as for data.

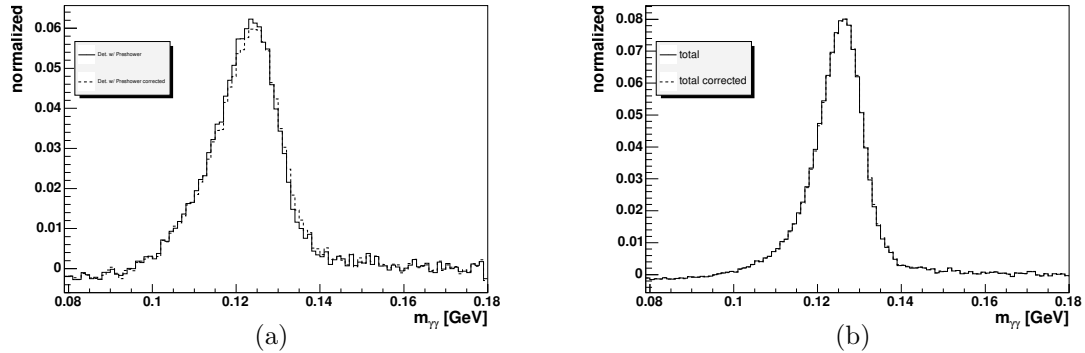


**Figure 5.20:** Comparison between  $m_{\gamma\gamma}$  distributions for Monte Carlos simulated events before and after the photon cluster energy correction. **(a)** detected-w/-preshower, **(b)** total.

The fact that no effect is visible for the  $m_{\gamma\gamma}$  distributions does not lead to the conclusion that the method of the correction is not adequate. In section 5.2 it was shown that an improvement of the photon energy resolution is possible. In case of  $\pi^0$ s the positive effect is canceled by the combination of two photons. For a

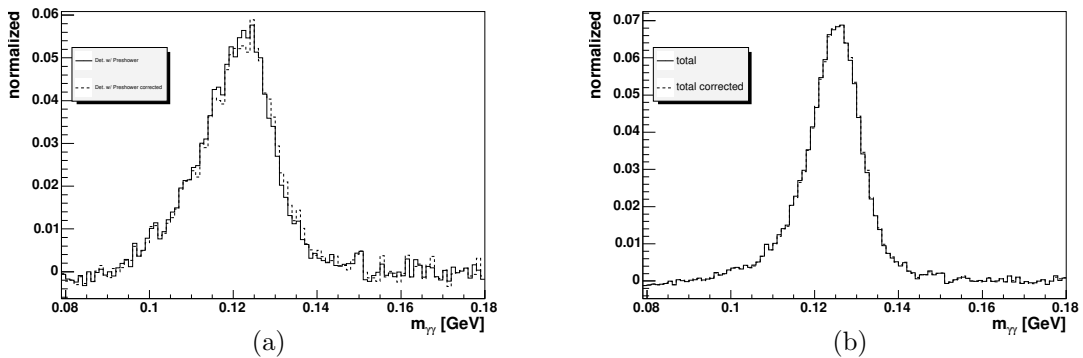


**Figure 5.21:** Comparison between  $m_{\gamma\gamma}$  distributions for data before and after the photon cluster energy correction. **(a)** detected-*w/-preshower*, **(b)** total.

*detected-w/-preshower*  $\pi^0$ -mesons which is influenced by the correction, only one photon is required to be assigned to the *detected-w/-preshower* sample. The other photon can be tagged as *detected-w/o-preshower*. Thus, the effect of the photon energy correction is expected to be smaller as for the basic photon distribution.

It might be possible that a specific optimization of the parameters  $A_{max}$  and  $N_{max}$  for a higher identification efficiency of photons which started to shower in front of the calorimeter would lead to an improvement of the resolution also for the  $m_{\gamma\gamma}$  distribution.

## 5.4 Summary

In this chapter two approaches to use the information delivered by the DIRC were presented. The first option was to study possible improvements on the photon energy resolution by discriminating preshower photons from photons which reached the EMC. The preshower photon sample shows a large asymmetry, while the asymmetry of the distribution of photons which reached the EMC is reduced compared with the total distribution. The same effect is visible for the resolution of the reconstructed  $\pi^0$  mass for the considered generic  $B^0\bar{B}^0$  sample as well as for data. A relative improvement of the  $\pi^0$  mass resolution of 5.4% is achieved for the simulated events and 4.7% for data.

The second application of the identification of preshower photons is an energy correction depending on the number of Cherenkov photons associated to a photon cluster. Based on generator level information delivered by the Monte Carlo simulation a correlation between the energy loss of photons and the number of associated Cherenkov photons was found. The determined correction constants were applied in energy and polar angle intervals. It was proved that the method is functioning by repeating the algorithm on photon clusters with an already corrected energy. The corrected distribution of preshower photons is much more symmetric compared with the distribution before the correction. The resolution of the total corrected distribution shows a relative improvement of 1% compared with the total distribution before correction. However, the application of the energy correction shows no effect on the resolution of the reconstructed  $\pi^0$  mass with the current performance of the preshower identification method.

# Chapter 6

## Conclusion and outlook

### 6.1 Conclusion

The aim of this study was to identify photons which started electromagnetic showers before reaching the calorimeter, due to interactions with material of the inner components of the *BABAR* detector. *BABAR*'s Cherenkov detector (DIRC) has been successfully used to identify preshowers: The number of DIRC Cherenkov photons associated to an electromagnetic calorimeter cluster allows to identify clusters with preshowers. The detection efficiency is about 50%, that means, it is possible to reduce the fraction of photons with preshowers from 13% to 7.4%. The resulting improvement of the photon energy resolution is 2.9%. The resolution of the reconstructed  $\pi^0$ -mass could be improved by 5% by rejecting clusters with preshowers. The results are consistent on data and Monte Carlo simulations.

Further studies showed that an energy correction depending on the number of detected Cherenkov photons associated to a photon cluster is possible. An improvement of 1% was achieved for the photon energy resolution. With the current performance of preshower detection and energy correction no improvement for the  $\pi^0$ -mass resolution has been found.

These results have been presented to the *BABAR* collaboration. It is planned to integrate the modifications of the *BABAR* software which was developed for this study into the official *BABAR* software. The improvements to the photon energy resolution and a tool to study systematic uncertainties is now available to the *BABAR* collaboration.

### 6.2 Outlook

Since the feasibility of the association was not clear at the beginning, this study was restricted to isolated calorimeter clusters. It should be studied if the association is still possible with a less tight isolation requirement which would increase the number of clusters which are considered for association.

The optimization of the selection of detected Cherenkov photons was done with maximum efficiency and minimal pollution of both samples, with and without preshowers, in mind. A specific selection to optimize efficiency and pollution only of the clusters with preshowers, not regarding the sample without detected preshowers, might lead to improved results for the energy correction. On the other hand, a specific selection to optimize efficiency and pollution of the clusters without preshowers (again, not regarding the other sample, with preshowers) would lead to a much refined sample after preshower rejection. In other words, two separate selections, one optimized for preshower rejection and the other optimized for preshower energy correction would improve the results.

# Bibliography

- [1] J.H. Christenson, J.W. Cronin, V. Fitch, R. Turlay, Phys. Rev. Lett. **13** 138 (1964).
- [2] S. Eidelman *et al.*, Phys. Lett. Meth. B **592**, 1 (2004).
- [3] M. Kobayashi, T. Maskawa, Prog. Theor. Phys. **49** 652 (1973).
- [4] W.R. Leo, “Techniques for Nuclear and Particle Physics Experiments”, Springer Verlag (1994)
- [5] B. Aubert *et al.* [*BABAR* Collaboration], Nucl. Instrum. Meth. A **479**, 1 (2002).
- [6] P.F. Harrison, H.R. Quinn, The *BABAR* Physics Book – Physics at an Asymmetric *B* Factory, SLAC-R-504 (1998).
- [7] A. Höcker *et al.*, ”THE DIRC TIMING”, *BABAR*DIRC Note **135** (2000)
- [8] D.J. Lange, Nucl. Instrum. Meth. A **462**, 152 (2001).
- [9] S. Giani *et al.*, Geant – Detector Description and Simulation Tool, CERN Program Library Long Writeup W5013 (1994).
- [10] F. James, MINUIT – Function Minimization and Error Analysis, CERN Program Library Long Writeup D506 (1994).
- [11] J. Marks, Private Communication (2004)
- [12] J. Marks, Private Communication (2004)



# Danksagung

An dieser Stelle möchte ich mich bei all denjenigen sehr herzlich bedanken, die mich während meiner Diplomarbeit unterstützt haben.

Besonderer Dank gilt:

- Prof.Dr. Ulrich Uwer für ein spannendes und interessantes Thema, für die hilfsbereite Unterstützung und für ein immer offenes Ohr für alle Fragen.
- Dr. Rolf Dubitzky für die intensive Betreuung und Hilfestellung in allen Situationen.
- Dr. Jörg Marks für die zahlreichen und interessanten Diskussionen.
- Stefan Schenk für manchen hilfreichen Hinweis und die häufige Hilfe bei “organisatorischen” Fragen.
- Johannes Albrecht für das gute Zusammenleben im gemeinsamen Büro.
- Dr. Michael Walter für die Erleichterung des Einlebens zu Beginn meiner Arbeit.
- der ganzen HE-Gruppe für die abwechslungsreiche Zeit.
- meiner Familie für die Ermöglichung meines Studiums.



# Erklärung

Ich versichere, dass ich diese Arbeit selbständig verfaßt und keine anderen als die angegebenen Quellen und Hilfsmittel benutzt habe.

Heidelberg, den 31. Januar 2005

-

---